

FORMATION OF CLOSE BINARIES THROUGH MASSIVE BLACK HOLE PERTURBATIONS AND CHAOTIC TIDES

HOWARD HAO-TSE HUANG^{ID}

Department of Astronomy, University of California at Berkeley, Berkeley, CA 94720, USA

WENBIN LU^{ID}

Department of Astronomy, University of California at Berkeley, Berkeley, CA 94720, USA

Version November 18, 2025

Abstract

Hills breakup of binary systems allows massive black holes (MBH) to produce hyper-velocity stars (HVSs) and tightly bound stars. The long timescale of orbital relaxation means that binaries must spend numerous orbits around the MBH before they are tidally broken apart. Repeated MBH tidal perturbations over multiple pericenter passages can perturb the binary inner orbit to high eccentricities, leading to strong tidal interactions between the stars. In this work, we develop a physical model of the MBH-binary system, taking into account outer orbital relaxation, MBH tidal perturbations, and tidal interactions between the binaries in the form of dynamical tides. We show that when the inner orbit reaches high eccentricities such that the pericenter radius is only a few times stellar radii (R_*), the stellar oscillation modes can grow chaotically and rapidly harden the binaries to semi-major axes $a_b \lesssim 10 R_*$. We find that a significant fraction (up to 50%) of initially wide binaries that are in the empty loss-cone regime ($a_b \sim 1.0$ AU) do not undergo Hills breakup as wide binaries, but instead experience chaotic growth of tides and become close binaries. These tidally hardened binaries provide a new channel for the production of the fastest HVSs, and are connected to other nuclear transients such as repeating partial tidal disruption events and quasi-periodic eruptions.

1. INTRODUCTION

The well-known outcome from the tidal breakup of a binary system by a massive black hole (MBH) is that one star (with positive energy) is ejected to infinity as a hyper-velocity star (HVS; Brown 2015) and that the other one (with negative energy) is left bound to the MBH. The original work of Hills (1988) and many subsequent works (e.g., Yu and Tremaine 2003; Bromley *et al.* 2006; Sari *et al.* 2010; Rossi *et al.* 2014; Generozov and Madigan 2020; Yu and Lai 2024) only considered the idealized case that a binary remains unperturbed before the tidal breakup, which is only true if the breakup occurs in one outer orbit. However, in reality, the binary's outer orbit undergoes a large number of pericenter passages¹ (driven by relaxation) before the final breakup and, during this time, the binary's inner orbit can be significantly modified by the MBH's tidal perturbations combined with tidal interactions between the two stars.

Recently, Bradnick *et al.* (2017) considered multiple pericenter passages along with relaxation of the outer orbit. They found that the inner eccentricity can be excited by the cumulative perturbations of the MBH's tidal forces, and they concluded that most binaries undergo collisions instead of tidal breakups. Stephan *et al.*

haotse813@berkeley.edu
 wenbinlu@berkeley.edu

¹ A binary system that is initially on a parabolic orbit may also undergo multiple pericenter passages due to the energy exchange between inner and outer orbits (see Sersante *et al.* 2025).

(2019) also considered multiple outer orbits in the eccentric Kozai-Lidov (eKL) framework and found that the eKL mechanism can induce high inner eccentricities and lead to stellar collisions/mergers.

These two works mentioned above assumed that the the tidal circularization of the inner orbit is due to damping of the time-dependent equilibrium tide (e.g., Zahn 1977; Hut 1981; Eggleton *et al.* 1998). In reality, at sufficiently high inner eccentricities (e.g., when the inner pericenter is less than a few stellar radii), we expect the encounters between the two stars to excite strong dynamical tides. Moreover, if the tidally excited modes lead to significant change in the inner orbital period, the pericenter passages may occur at random oscillation phases such that the system is in the chaotic regime (Kochanek 1992; Mardling 1995). This leads to rapid growth of the mode amplitude, and the rapid shrinkage of the inner semi-major axis causes the inner orbit to decouple from the outer orbit and hence a violent collision can be avoided. Such chaotic tides have been considered in the orbital migration of hot Jupiter planets in close orbits around host stars (Wu 2018; Vick and Lai 2018). Similarly, we expect binary stars that have undergone chaotic tides to evolve into very close inner orbits.

Tidal breakup of close binaries will deliver the bound stars extremely close to the MBH. Although the fate of these bound stars from Hills breakup are uncertain (Sari and Fragione 2019; Lu *et al.* 2021; Linial and Sari 2023), they may be responsible for quasi-periodic

eruptions (QPEs) and repeating partial tidal disruption events (TDEs) (e.g., [Miniutti et al. 2019](#); [Giustini et al. 2020](#); [Arcodia et al. 2021](#); [Payne et al. 2021](#); [Cufari et al. 2022](#); [Lu and Quataert 2023](#); [Linial and Metzger 2023](#); [Yao and Quataert 2025](#); [Makrygianni et al. 2025](#); [Pasham et al. 2024](#); [Chakraborty et al. 2025](#)). A significant fraction of close binaries may also undergo double tidal disruptions if the pericenter radius of the outer orbit is smaller than the tidal disruption radii of both stars ([Mandel and Levin 2015](#)).

In this paper, we study the long-term evolution of binary stars including the effects of outer orbital relaxation, tidal perturbations of the inner orbit by the MBH, and dynamical tides excited by the mutual tidal interactions between the two stars. We quantify the fractional outcomes of tidal breakup, collisions/mergers, and chaotic tides. Our main findings are: (1) the repeated MBH perturbations on the binary during the stochastic outer orbit relaxation can drive the binary’s inner orbit to high eccentricities, and (2) a significant population of wide binaries, instead of undergoing Hills breakup or collisions, may experience the chaotic growth of tides and become close binaries. Near the completion of this paper, we notice another complementary work by [Dodici et al. \(2025\)](#) who proposed that perturbations of the inner eccentricity due to fly-bys of field stars may also trigger chaotic tides, so there are multiple channels of making close binaries via chaotic tides.

This paper is organized as follows. In Section 2 we introduce our physical model of the MBH-binary system. Our results of individual systems and population study are presented in Section 3. We discuss the limitation and implications of our model in Section 4, and conclude our findings in Section 5.

2. METHODS

We consider a binary system on a highly eccentric Keplerian orbit around a MBH. Throughout this paper, we take our own Galactic Center as an example, with MBH mass $M_{\text{BH}} = 4.26 \times 10^6 M_{\odot}$ ([GRAVITY Collaboration et al. 2020](#)). The binary system consists of two zero-age-main-sequence (ZAMS) stars of mass $M_* = 0.5 M_{\odot}$ and radius $R_* = 0.478 R_{\odot}$. Our framework is general and can be applied to other MBH and stellar masses as well. In this hierarchical three-body system, we refer to the orbit between the two stars as the inner orbit, and the orbit of the binary system around the MBH as the outer orbit. In this paper, we denote the orbit elements of the inner orbit with an additional subscript b to distinguish them from those of the outer orbit. When necessary, $_{*,1}$ and $_{*,2}$ are used to emphasize the properties of the first and second stars in the system. The evolution of the binary system is governed by three pieces of physics: (1) the outer orbit relaxation by the gravitational encounters with other field stars, (2) the inner orbit perturbation by the MBH tides during the pericenter passage of the outer orbit, and (3) the influence of the stellar tides on dynamics of the inner orbits. The interaction between MBH and the binary is further affected by the various precessions. The details of the precessions are described separately in Appendix A.

Figure 1 provides an overview of the physics in the system. On a long timescale over many outer orbits, the binary experiences gravitational interactions with other

stars and its outer orbit gradually relaxes. As a result, the outer pericenter r_p may decrease for some systems. The MBH tides will overwhelm the inner orbit and lead to Hills breakup if r_p is reduced to a few times the tidal breakup radius ([Hills 1988](#)):

$$r_t = a_b \left(\frac{M_{\text{BH}}}{M_b} \right)^{1/3}, \quad (1)$$

where a_b is the SMA of the inner orbit and $M_b = M_{*,1} + M_{*,2} = 2 M_*$ is the total mass of the binary system.

However, before r_p reaches a few $\times r_t$, the perturbation of MBH tides on the inner orbit will already accumulate over several outer orbits and cause a change in the inner eccentricity e_b ². When e_b is driven to very large values, strong tidal interactions between two binary stars can happen, and in the most extreme case the two stars will collide. If the inner pericenter radius $r_{p,b}$ is only a few times R_* , the tidal forces between the two stars will excite the stellar oscillation modes and transfer the orbital energy to the stellar oscillations ([Press and Teukolsky 1977](#); [Kochanek 1992](#)). With sufficiently small $r_{p,b}$ and large energy kicks, the amplitudes of the stellar oscillation can grow chaotically and lead to a rapid shrinkage of the inner orbit within one outer orbit ([Wu 2018](#); [Vick and Lai 2018](#)). The production of hardened binaries has several interesting implications, which are discussed in Section 4.3.

In the following sections, we elaborate on those pieces of physics and how they are integrated into our MBH-binary model.

2.1. Outer orbit relaxation

Consider a binary system on an eccentric outer orbit, with the specific angular momentum \mathbf{L} , energy E_{orb} , and eccentricity vector \mathbf{e} . Due to gravitational encounters with other stars, \mathbf{L} and E_{orb} will gradually change. For highly eccentric orbits, the angular momentum relaxation timescale $t_{L,\text{relax}}$ is usually smaller than the energy relaxation timescale $t_{E,\text{relax}}$ ([Sari and Fragione 2019](#)). Furthermore, since the MBH perturbation on the inner orbit is determined mostly by r_p that changes on the timescale $t_{L,\text{relax}}$, we only consider the relaxation of \mathbf{L} and fix E_{orb} to its initial value.

In highly eccentric orbits, the position of the binary \mathbf{r} is nearly parallel to the eccentricity vector \mathbf{e} most of the time, so gravitational encounters causing velocity deflections mainly change \mathbf{L} in the direction perpendicular to \mathbf{e} . More specifically, the angular momentum change $\Delta \mathbf{L}$ per outer orbit lies in the plane spanned by $\hat{\mathbf{L}}$ and $\hat{\mathbf{L}} \times \hat{\mathbf{e}}$, where $\hat{\mathbf{L}}$ and $\hat{\mathbf{e}}$ are the unit vector in the directions of \mathbf{L} and \mathbf{e} . Given the period of the outer orbit $P(a) = 2\pi\sqrt{a^3/GM_{\text{BH}}}$ and the two-body relaxation time $t_{2B,\text{relax}}$, we model $\Delta \mathbf{L}$ as follows³

$$\Delta \mathbf{L} = L_c(a) \sqrt{\frac{P(a)}{t_{2B,\text{relax}}}} \left(c_1 \hat{\mathbf{L}} + c_2 \hat{\mathbf{L}} \times \hat{\mathbf{e}} \right), \quad (2)$$

where $L_c(a) = \sqrt{GM_{\text{BH}}a}$ is the angular momentum for a

² For $r_p \lesssim 10 r_t$, a_b can also be perturbed due to the chaotic three-body interaction (see Section 2.2).

³ Our treatment of the outer orbit diffusion differs from [Bradnick et al. \(2017\)](#).

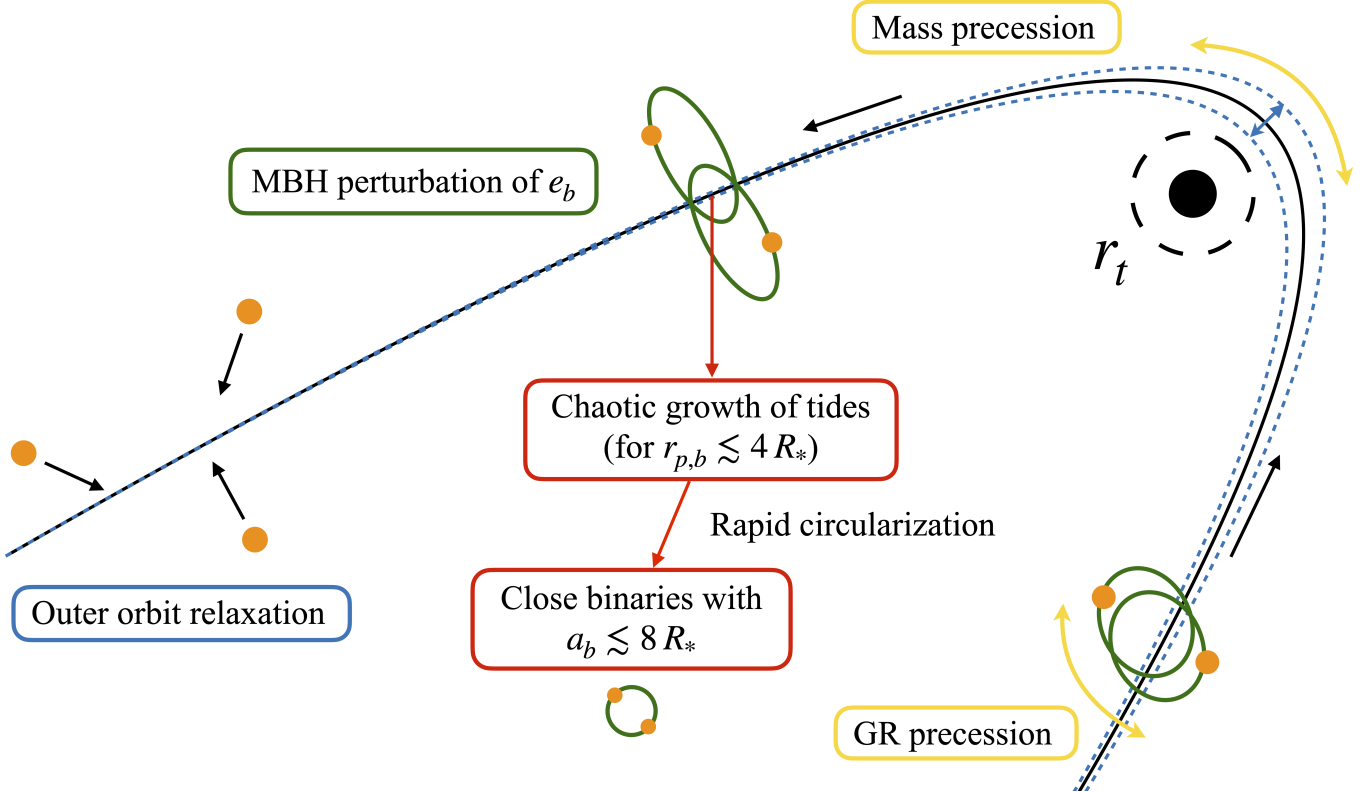


FIG. 1.— Overview of the physical processes in the MBH-binary three-body system. The binary system is on a highly eccentric orbit around the MBH. On a timescale of $t_{L,\text{relax}}$ (eq. 6), the outer pericenter radius r_p gradually changes because of the gravitational encounter with other field stars. In our simulation, the gravitational encounters are not resolved; instead, the outer orbit relaxation is handled using a simplified version of Fokker-Planck formulation (Section 2.1). Every time the binary passes through the pericenter around the MBH, its inner eccentricity is perturbed by the MBH's tidal forces (Section 2.2). When the inner eccentricity e_b grows to a sufficiently large value, two binary stars start to interact tidally near the inner pericenter, which causes the energy transfer between the inner orbit and the stellar oscillations. Under certain conditions (eq. 8), the stellar mode amplitude will grow chaotically, leading to the rapid hardening of the binary system (Section 2.3). Finally, there exists various precessions that can affect the MBH perturbations on e_b (Appendix A).

circular outer orbit, and c_1, c_2 are two random numbers drawn independently from the normal distribution with zero mean and unit variance.

The per-outer-orbit change in the magnitude of angular momentum ΔL can also be recovered from Eq. (2):

$$\langle \Delta L \rangle = \sum_i \frac{L_i}{L} \langle \Delta L_i \rangle + \sum_{ij} \frac{1}{2L} \left(\delta_{ij} - \frac{L_i L_j}{L^2} \right) \langle \Delta L_i \Delta L_j \rangle = \frac{L_c^2(a)}{L} \frac{P(a)}{t_{2B,\text{relax}}}, \quad (3)$$

$$\langle (\Delta L)^2 \rangle = \sum_{ij} \frac{L_i L_j}{L^2} \langle \Delta L_i \Delta L_j \rangle = L_c^2(a) \frac{P(a)}{t_{2B,\text{relax}}}. \quad (4)$$

Therefore, the random walk of \mathbf{L} as modeled by eq. (2) automatically incorporates both the drift $\langle \Delta L \rangle$ and diffusion $\langle (\Delta L)^2 \rangle$ of the magnitude of angular momentum L .

In principle $t_{2B,\text{relax}}$ depends on the radial number density profiles of the stars and other compact objects at the galactic center, and is a function of radius r . However, since those profiles are not well-constrained within the central parsec of the galactic center, we use a fixed value of $t_{2B,\text{relax}}$ for a given system (see Section 2.4). The required number of outer orbits to change L significantly

can be obtained from $t_{2B,\text{relax}}$:

$$N_l \sim \frac{L^2}{\langle (\Delta L)^2 \rangle} = \frac{L^2}{L_c^2(a)} \frac{t_{2B,\text{relax}}}{P(a)} \approx \frac{2r_p}{a} \frac{t_{2B,\text{relax}}}{P(a)} = 2.4 \times 10^3 \left(\frac{a_b}{1 \text{ AU}} \right) \left(\frac{r_p}{70 r_t} \right) \left(\frac{t_{2B,\text{relax}}}{1 \text{ Gyr}} \right) \left(\frac{a}{1 \text{ pc}} \right)^{-5/2}. \quad (5)$$

The corresponding angular momentum relaxation timescale is

$$t_{L,\text{relax}} = N_l P \approx \left(\frac{2r_p}{a} \right) t_{2B,\text{relax}}. \quad (6)$$

2.2. MBH tidal perturbations

During the outer pericenter passage, the binary's inner orbit is perturbed by the MBH tides. Depending on the orbit orientation, e_b can either increase or decrease. The effect of the perturbation can be roughly divided into two regimes:

1. For $r_p \gtrsim 10 r_t$, the MBH perturbation primarily affects e_b while keeping a_b largely unchanged. Since the angular frequency of the inner orbit is much higher than that of the outer pericenter passage, the change in e_b occurs gradually over many inner

orbits, and the secular approximation can provide an analytical estimate of the total change in e_b and in the inner orbit orientation (Hammers and Samsing 2019). We adapt the result of Hammers and Samsing (2019) in the parabolic encounter limit ($e = 1$) to approximate our highly eccentric outer orbits. The full analytical expression of the inner orbit perturbation is given in Appendix D. If the outer orbit does not undergo relaxation, the repeated perturbations over multiple outer orbits become the eKL effect, where e_b can be driven to near unity (see the review by Naoz 2016). However, since the outer orbit of the binary system is constantly under relaxation, the change in e_b is stochastic over many outer orbits and cannot be analytically described.

2. For $r_p \lesssim 10 r_t$, the effect of MBH tides on the binary system is increasingly chaotic. As the angular frequency of the outer pericenter passage becomes comparable to that of the inner orbit, the secular approximation breaks down. We resolve this complex three-body interaction with the N-body simulation code REBOUND with the IAS15 integrator (Rein and Liu 2012; Rein and Spiegel 2015). Since the tidal interaction between the MBH and the binary is concentrated near the outer pericenter, we only integrate the section of the orbit where the distance between the MBH and the binary is less than $10 \times \max(r_t, r_p)$.

Figure 2 shows two examples of the evolution of binary separation $r_b(t)$ near one outer pericenter passage. Initially r_b changes periodically due to the non-zero inner eccentricity. As the binary passes through the outer pericenter, the inner orbit gets perturbed by the MBH. For $r_p = 6.0 r_t$ (upper panel), the change in e_b and $r_{p,b}$ is relatively smooth, while for $r_p = 3.0 r_t$ (lower panel), the change is more abrupt. Furthermore, for $r_p = 3.0 r_t$, the binary separation can briefly reach below $2 R_*$ during the outer pericenter passage and lead to binary collision. This highlights the importance of resolving the three-body dynamics explicitly, since the collision can only be detected by constantly monitoring the binary throughout the MBH perturbation. For $r_p \lesssim 3 r_t$, the MBH perturbation can also result in the Hills breakup. This outcome is captured in our REBOUND simulations, where we measure the velocity v_{HVs} of the ejected star and the orbital properties of the bound star.

2.3. Chaotic tides and inner orbit dynamics

The tidal interactions between binary stars can be significant when $r_{p,b}$ is small. One popular method of modeling the tidal interactions is to only consider equilibrium tides, where the stars are assumed to be in instantaneous hydrostatic equilibrium with the tidal field of the companions (Hut 1981; Eggleton *et al.* 1998; Eggleton and Kiseleva-Eggleton 2001). Although this approach has been used in previous works (Bradnick *et al.* 2017; Stephan *et al.* 2019), it neglects the dynamical and oscillatory nature of tides. Specifically, when e_b is sufficiently high and $r_{p,b}$ is only a few times R_* , the tidal force of the companion can excite the stellar oscillation modes during the inner pericenter passage and transfer a fraction of the orbital energy to the oscillation modes. This

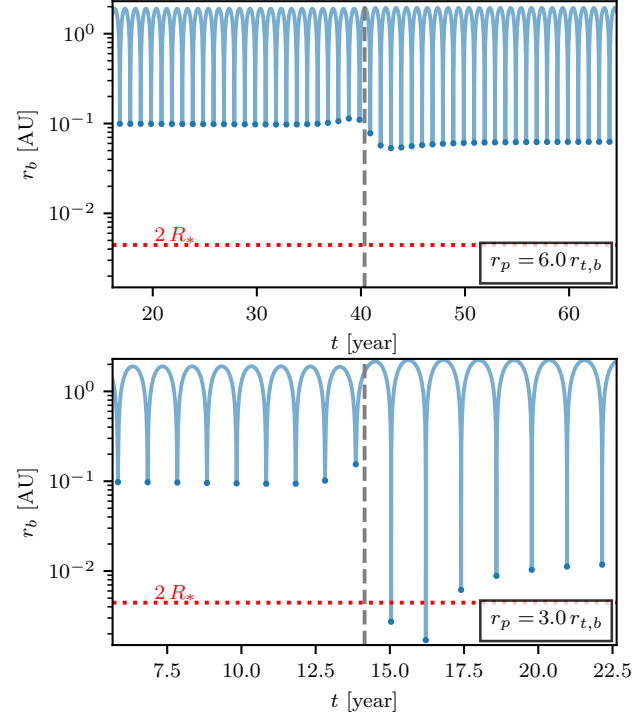


FIG. 2.— The binary separation $r_b(t)$ as a function of time. The binary system is on an eccentric orbit around the MBH, with $a = 0.5 \text{ pc}$ and $r_p = 6.0 r_t$ (upper panel), $3.0 r_t$ (lower panel). The inner orbit has initial SMA $a_{b,0} = 1.0 \text{ AU}$ and eccentricity $e_{b,0} = 0.9$. The outer orbit has \mathbf{L} in $+\hat{z}$ direction and pericenter on $-\hat{x}$ axis. The initial orientation of the binary system are specified by the orbital elements $i_{b,0} = 0.7\pi$ (inclination angle), $\omega_{b,0} = 0.1\pi$ (argument of pericenter), $\Omega_{b,0} = 0.95\pi$ (longitude of ascending node), and $M_{b,0} = 1.0$ (mean anomaly). The gray vertical line marks the time of the outer pericenter passage, the red horizontal line is the sum of the two binary star's radii, and the inner pericenter radii are highlighted with circular markers. For $r_p = 3.0 r_t$ (bottom panel), the binary separation and inner pericenter radii drop below $2 R_*$ temporarily near the outer pericenter, which highlights the sharp change in e_b when r_p is small. In our simulation, the binary system on the lower panel is flagged as collision as soon as the binary separation becomes less than $2 R_*$.

energy transfer between orbit and stellar oscillation was first investigated in the tidal capture of binary systems (Press and Teukolsky 1977; Kochanek 1992; Mardling 1995). Mardling (1995) demonstrated that when $r_{p,b}$ is sufficiently small, the modulation of the orbital period due to energy transfer will cause the oscillation mode to receive kicks at effectively random phases during pericenter passages. The random kicks in the stellar oscillation over multiple orbits will lead to its chaotic growth, during which the orbital energy is quickly drained and the binary is hardened efficiently. The efficient hardening from chaotic tides has been proposed to explain the migration of the hot Jupiters (Wu 2018; Vick and Lai 2018). For high e_b , the tidal interaction is localized near the pericenter passage, and the mode energy evolution over multiple inner orbits can be described using an iterative map (Vick and Lai 2018). In the following, we describe our use of the iterative map to solve the interactions between stellar oscillation modes and orbital dynamics self-consistently.

In our model we only consider a single stellar oscillation mode, the $l = m = 2$ f -mode, in Star 1, while ignoring all modes in Star 2 (to be conservative in our model). We

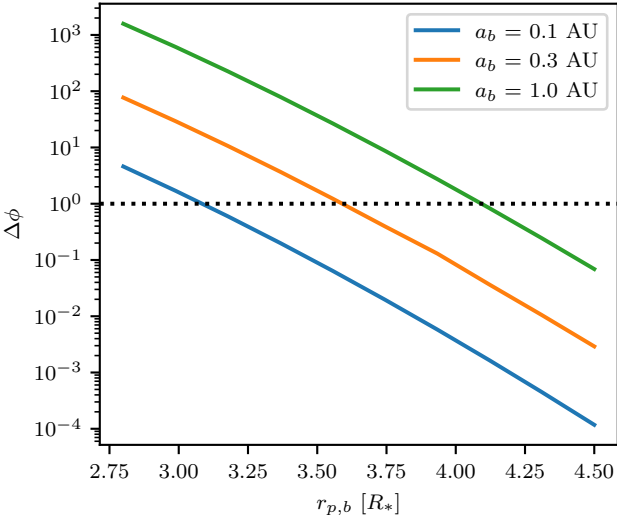


FIG. 3.— The change in the stellar oscillation phase (Eq. 8) due to the variation in inner orbital period after the energy kick from the inner pericenter passage. The horizontal line, $\Delta\phi = 1$, is the crude requirement for triggering the chaotic tides. The intersections between this horizontal line and the curves are $r_{b,ct}$. Depending on the value of a_b , $r_{b,ct}$ ranges from 3 to $4 R_*$.

use MESA (Paxton *et al.* 2011, 2013, 2015, 2018, 2019; Jermyn *et al.* 2023) to produce the stellar model, and then post-process it with GYRE (Townsend and Teitler 2013) to compute the eigenfunction and eigenfrequency of the stellar oscillation modes. The $l = m = 2$ f -mode has angular frequency ω_f and initial complex amplitude $A_f = 0$. The amplitude is normalized such that the energy and angular momentum stored in the mode are $E_f = |A_f|^2$ and $L_f = 2|A_f|^2/\omega_f$. Let the subscript k denotes the quantities right before the k -th inner pericenter passages. The iterative map of the complex amplitude A_f is given by (Vick and Lai 2018):

$$A_{f,k+1} = (A_{f,k} + \Delta A_{f,k}) e^{i\omega_f P_{b,k+1}}, \quad (7)$$

where $P_{b,k}$ is the period of the k -th inner orbit, and ΔA_k describes the kick from the tidal force during the k -th pericenter passage. The value of $\Delta A_{f,k}$ depends strongly on the $r_{p,b}$ and weakly on e_b . A more detailed description of the iterative map and the expression for $\Delta A_{f,k}$ is provided in Appendix B.

The chaotic growth in A_f requires that the consecutive kicks happen at random phases. With zero initial mode energy, this requirement is roughly given by (Wu 2018; Vick and Lai 2018):

$$1 \text{ rad} < \Delta\phi = \omega_f |P_{b,1} - P_{b,0}| = \frac{3}{2} \omega_f P_{b,0} \left| \frac{\Delta E_{f,0}}{E_{b,\text{orb},0}} \right|, \quad (8)$$

where $E_{b,\text{orb},0}$ is the initial inner orbital energy and $\Delta E_{f,0} = |\Delta A_{f,0}|^2$ is the initial energy kick. We assume that the fractional change in period is small ($|\Delta E_{f,0}| \ll |E_{b,\text{orb},0}|$) to obtain eq. (8). Figure 3 shows $\Delta\phi(r_{p,b})$ for $a_b = 0.1, 0.3, 1.0$ AU for the first pericenter passage. The steepness of the function reflects the sensitivity of $\Delta E_{f,0}$ to $r_{p,b}$. For a given a_b , we define the critical radius of chaotic tides $r_{b,ct}$ as

$$\Delta\phi(r_{p,b} = r_{b,ct}) = 1. \quad (9)$$

This is the rough radius at which the chaotic tides are

triggered, with $r_{b,ct} = 3 \sim 4 R_*$ for a_b ranging from 0.1 to 1 AU.

Once chaotic tides are triggered, E_f will grow, on average, as

$$\langle E_f \rangle \sim N_b \Delta E_{f,0}, \quad (10)$$

where N_b is the number of inner orbits. The large phase change $\Delta\phi$ required to trigger the chaotic tides (eq. 8) can be translated into a minimum growth rate:

$$E_f \gtrsim N_b \cdot \frac{2}{3} \frac{|E_{b,\text{orb},0}|}{\omega_f P_{b,0}}. \quad (11)$$

The number of inner orbits for E_f to grow to $0.1 |E_{b,\text{orb},0}|$ is

$$N_b \lesssim 0.15 \omega_f P_{b,0} = 1.1 \cdot 10^4 \left(\frac{a_b}{1.0 \text{ AU}} \right)^{3/2}. \quad (12)$$

As we mainly consider binaries on wide outer orbits with $P/P_b = 4.5 \times 10^4 (a/\text{pc})^{3/2} (a_b/\text{AU})^{-3/2}$, we find that chaotic tides, once triggered, will most likely shrink the inner orbit within one outer orbit. If so, the inner orbit evolution will rapidly decouple from the outer orbit — this rapid decoupling is not correctly captured in previous works Bradnick *et al.* (2017); Stephan *et al.* (2019).

In our model, we check for the onset of chaotic tides once per outer orbit using the iterative map. After applying the MBH perturbation at the outer pericenter (Section 2.2), the updated a_b and e_b serve as initial conditions for the map (Eq. 7) to evolve E_f . The maximum number of iteration steps is (conservatively) set to $0.9 \times P/P_b$ inner orbits. When E_f exceeds $0.3 |E_{b,\text{orb},0}|$, we consider the binary to have undergone significant orbital shrinkage and triggered chaotic tides. Our results are insensitive to the exact choice of $0.3 |E_{b,\text{orb},0}|$, because the model energy grows extremely rapidly when chaotic tides are triggered. The subsequent orbital evolution is not included in our model, but is discussed in Sections 4.2 and 4.3.

2.4. Model parameters and potential outcomes

The parameters used in our fiducial models are listed in Table 1. Our MBH-binary model incorporates the physics of two-body relaxation, tidal interaction between two stars, and MBH perturbation of the inner orbit. We also include the effects of Schwarzschild and mass precessions, which are described in detail in Appendix A. We consider three choices of initial inner SMA $a_{b,0} = 0.1, 0.3, 1.0$ AU. For each $a_{b,0}$, we further select initial inner eccentricity $e_{b,0}$ from nine evenly spaced values in the range $[0.1, 1 - 8R_\odot/a_{b,0}]$. This avoids very small $r_{p,b} < 8R_\odot$ and prevents our statistics from being biased by those binaries that are already close to collision/triggering of chaotic tides. The initial inner orbital orientation is determined by the longitude of ascending node Ω_b , inclination i_b , and the argument of pericenter ω_b , for which we randomly sample from uniform distributions in the ranges $\Omega_b \in [0, 2\pi]$, $\cos i \in [-1, 1]$, $\omega_b \in [0, 2\pi]$. The outer orbit is initialized in the xy plane, with the angular momentum in $+\hat{z}$ direction and pericenter on the $-\hat{x}$ axis.

We consider two choices of outer SMA $a = 0.5, 2.0$ pc. The initial outer pericenter radius $r_{p,0}$ is fixed to $70 r_t$ to ensure that the MBH's influence on the inner orbit is

TABLE 1
PARAMETERS ADOPTED IN OUR FIDUCIAL MODELS.

Symbol	Values/Ranges	Description
M_*	$0.5 M_{\odot}$	Mass of each star
R_*	$0.478 R_{\odot}$	Radius of each star
\bar{Q}	0.1198	Dimensionless tidal coupling coefficient for $l = m = 2$ f -mode
ω_f	$1.67084 \sqrt{GM_*/R_*^3}$	Angular frequency for for $l = m = 2$ f -mode
$a_{b,0}$	0.1, 0.3, 1.0 AU	Initial inner SMA
$e_{b,0}$	$[0.1, 1 - 8 R_{\odot}/a_{b,0}]$	Initial inner eccentricity
η	0, 1	Power law index of the inner eccentricity distribution
M_{BH}	$4.26 \times 10^6 M_{\odot}$	MBH mass
a	0.5, 2.0 pc	Outer SMA
$r_{p,0}$	$70 t_{b,t}$	Initial outer pericenter radius
$t_{2\text{B},\text{relax}}$	1, 10 Gyr	Two-body relaxation time of the outer orbit

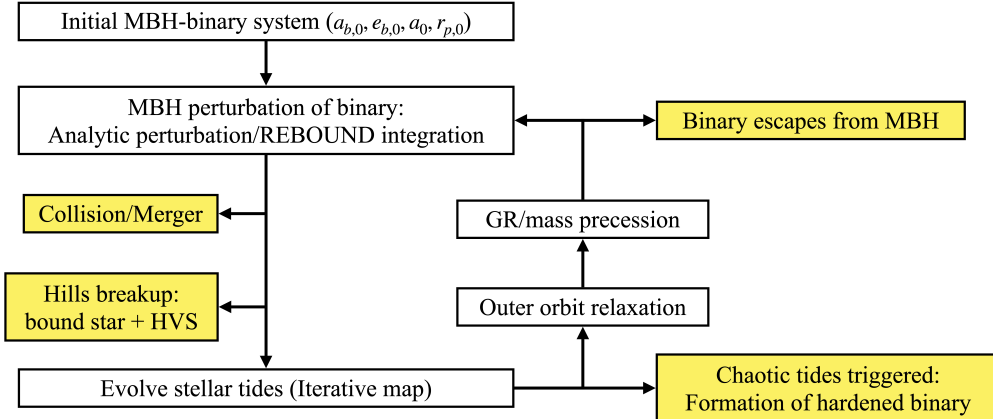


FIG. 4.— The simulation flow of our MBH-binary three-body system. The end states of the binary system are highlighted with yellow color. The simulation is stopped when the system reaches any of the end states, or when the total simulation time exceeds $0.1 t_{2\text{B},\text{relax}}$.

initially negligible. Two relaxation timescales $t_{2\text{B},\text{relax}} = 1, 10$ Gyr are used to account for the uncertainties in the density profiles at the galactic center.

For each set of $(a, t_{2\text{B},\text{relax}}, a_{b,0}, e_{b,0})$, 1000 binary samples are simulated to collect the statistics of different outcomes. Figure 4 illustrates the flow of the simulation cycle. The simulation steps are summarized as follows:

1. Initialize the inner orbit and outer orbit.
2. Simulate each outer pericenter passage and the MBH perturbation on the inner orbit. Depending on the size of r_p , this is handled differently:
 - For $r_p > 30 r_t$, the pericenter passage is not resolved and the perturbation to the inner orbit is computed with analytical secular approximation (see Section 2.2 and Appendix D).
 - For $r_p < 30 r_t$, the three-body interaction during the passage is numerically integrated with REBOUND package (Rein and Liu 2012; Rein and Spiegel 2015). This simulation is stopped if the binary stars collide or undergo Hills breakup.
3. Use the iterative map to evolve the stellar oscillation mode (see Section 2.3). The simulation is stopped if the chaotic tides are considered to be triggered.

4. Relax the outer orbit according to the method in Section 2.1. If $r_p > 175 r_t$ after the relaxation, the binary system is considered to be too far from the MBH and the simulation stops.
5. Update the inner and outer arguments of pericenter ω_b, ω with the Schwarzschild and mass precession, respectively (see Appendix A).
6. Repeat Step (2) to (5) until one of the stopping conditions is reached, or when the total simulation time reaches $0.1 t_{2\text{B},\text{relax}}$

3. RESULTS

In this section we present our results from Monte Carlo simulations. We first focus on the evolution of individual systems over multiple outer orbits, and illustrate the working of chaotic tides. We then show the statistics of the different outcomes, and their dependence on the initial orbital properties and the relaxation time. Finally, we present the statistics on the stellar collisions and the products of Hills breakup, including the orbital properties of HVS and bound stars.

3.1. Trajectories of MBH-binary system

We start by presenting the simulation results for individual systems. Figure 5 shows four example $(r_p, r_{p,b})$ trajectories. All systems have $(a, t_{2\text{B},\text{relax}}, a_{b,0}, e_{b,0}) = (0.5 \text{ pc}, 1 \text{ Gyr}, 1.0 \text{ AU}, 0.64)$. The four trajectories correspond to the four possible end states of the system, "Unbound from Hills breakup", "Trigger of chaotic tides",

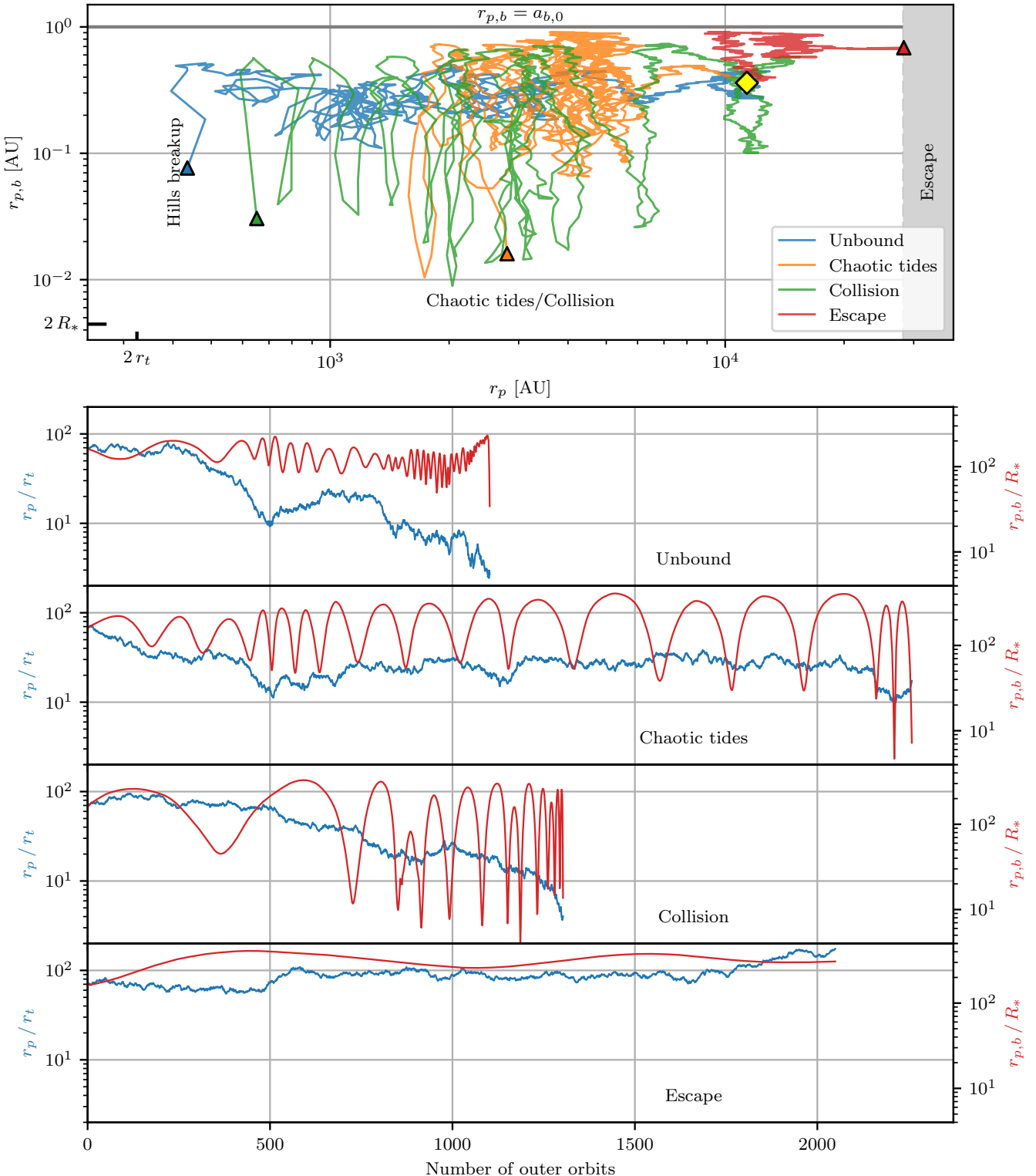


FIG. 5.— Example trajectories of the MBH-binary system. All systems have the same initial conditions $(a, t_{\text{2B,relax}}, a_{b,0}, e_{b,0}) = (0.5 \text{ pc}, 1 \text{ Gyr}, 1.0 \text{ AU}, 0.64)$. *Top panel:* The evolution of r_p and $r_{p,b}$. The initial state of the systems is marked with the yellow diamond. The states of the systems prior to the final outer pericenter passage are highlighted with triangles. *Bottom four panels:* r_p and $r_{p,b}$ evolution as the function of outer orbit number for the same trajectories as in the top panel. The random walk in r_p and the eKL-like oscillation can be clearly seen.

”Collision”, and ”Escape from MBH” (see also Figure 4). Qualitatively, the trajectory can be described as the combination of the random walk in r_p due to the outer orbit relaxation, and the the eKL-like movement in $r_{p,b}$ due to the MBH perturbation. If the former prevails, the binary will either undergo Hills breakup ($r_p \lesssim 3 r_t$) or escape from the tidal influence of the MBH ($r_p > 175 r_t$). Contrarily, if the latter excites e_b to a large value, the binary system may collide or experience chaotic tides. The end state of the binary system is controlled by the competition between these two stochastic processes. For most part of the trajectories, the change in a_b is negligible. However, significant change in a_b is still possible when $r_p \lesssim$ a few $\times r_t$ (Zhang *et al.* 2010).

3.2. Chaotic tides evolution

Figure 6 shows the evolution of a binary system that undergoes chaotic tides. The upper left panel plots a_b versus $r_{p,b}$ over multiple outer orbits and during the growth of chaotic tides. Before the final outer pericenter passage, the MBH repeatedly perturbs e_b with little change in a_b . This is reflected in the horizontal gray line. During the final outer pericenter passage, the MBH perturbs $r_{p,b}$ to $\sim 3.5 R_*$ and triggers the chaotic growth of stellar tides. The rapid growth of stellar tides shrinks a_b while keeping $r_{p,b}$ mostly unchanged, as shown by the red vertical line. The evolution of a_b and E_f during the chaotic growth of tides is shown in the lower left panel. It is clear that the increase in E_f is accompanied by the decrease in a_b due to the conservation of the total energy, and that the growth in E_f is not monotonic but diffusive. The right panel offers a more detailed look of the iterative map through the evolution of A_f (eq. 7).

3.3. Statistics of different binary outcomes

We next discuss the statistics of the three possible end states (excluding ”Escaped”; Figure 4) and their dependence on the initial conditions. We show that the emptiness of the loss cone provides a good indicator of the outcome statistics. We also examine the final r_p and demonstrate that chaotic tides can be triggered for $r_p \gtrsim$ a few $\times r_t$, where the MBH perturbation is still weak.

3.3.1. Empty versus full loss cone

The efficiency of angular momentum relaxation determines the number of outer orbits before the binary system reaches $r_p \sim r_t$ or escapes the influence of the MBH tides. This can be quantified by $\Delta l \equiv \Delta L/L_c$, the per-outer-orbit dispersion in the dimensionless angular momentum, and l_t , the dimensionless angular momentum at the binary tidal breakup radius:

$$\Delta l \equiv \Delta L/L_c = \sqrt{\frac{P}{t_{2B,relax}}}, \quad (13)$$

$$l_t \equiv L_t/L_c = \sqrt{1 - \left(1 - \frac{r_t}{a}\right)^2}, \quad (14)$$

where $L_c = \sqrt{GMa}$ is the angular momentum of a circular outer orbit, ΔL is the per-outer-orbit dispersion in the outer orbital angular momentum due to relaxation, and $L_t = \sqrt{GMa[1 - (1 - r_t/a)^2]} \approx \sqrt{2GMr_t}$ is

the critical angular momentum at which the binary will be tidally disrupted. For $\Delta l > l_t$, the binary system is in the full loss cone regime and r_p approaches r_t abruptly. For $\Delta l < l_t$, the binary system is in the empty loss cone regime and r_p approaches r_t in a gradual and diffusive way. Figure 7 shows Δl versus l_t for systems of different parameters (see Table 1). The black line indicates the boundary between empty and full loss cone regimes. Most of the systems in our model are in the empty loss cone regime, with a few of them close to the full loss cone regime.

3.3.2. Outcome statistics

We now present the statistics of different binary system outcomes. For a given set of $(a, t_{2B,relax}, a_{b,0})$, we weigh the cases from different initial inner eccentricities $e_{b,0}$ according to a power-law distribution:

$$p(e_{b,0}) \propto e_{b,0}^\eta, \quad (15)$$

where η is the power-law index. Two choices of η are used: 0 for a uniform distribution and 1 for the thermal distribution, although our results depend weakly on the choice of η (see later). Our statistics exclude the systems that are flagged as ”escaped” or do not reach any end states after $0.1 t_{2B,relax}$, which comprise 64 \sim 87 percents of the sample. Figure 8 shows the fractions of three different outcomes - collision f_{col} , unbound $f_{unbound}$ (Hills breakup), and chaotic tides f_{CT} . The fractions are normalized such that $f_{col} + f_{unbound} + f_{CT} = 1$. The outcome fractions are presented as a function of $\Delta l/l_t$, which quantifies the emptiness of the loss cone. Several features can be observed from Figure 8:

1. Independent of $\Delta l/l_t$ and $a_{b,0}$, stellar collisions are always subdominant, with f_{col} ranging from 10% to 25%. A similar fraction was found in Sersante *et al.* (2025).
2. For $\Delta l/l_t$ close to unity (full loss-cone regime), the Hills breakup dominates the outcome for all $a_{b,0}$ ($f_{unbound} \gtrsim 70\%$).
3. With decreasing $\Delta l/l_t$ (emptier loss-cone), there is a significant fraction of chaotic tides for $a_{b,0} \gtrsim 0.3$ AU. For $a_{b,0} = 1.0$ AU, f_{CT} can reach above 60% for $\Delta l/l_t < 0.1$. For small $a_{b,0}$ (very close binaries), f_{CT} remains low even for $\Delta l/l_t$ much less than unity.
4. The outcome fractions are insensitive to the power index η of the initial inner eccentricity distribution (eq. 15), with little difference between $\eta = 1$ (thermal) and 0 (uniform).

The trends of $f_{unbound}$ and f_{CT} with $\Delta l/l_t$ can be explained as follows. When $\Delta l/l_t$ is close to unity, r_p approaches r_t in only a few outer orbits and the cumulative MBH perturbation of e_b is weak. Therefore, most systems that do not escape will reach $r_p \sim$ a few $\times r_t$ and undergo Hills breakup. On the other hand, when $\Delta l/l_t$ is much less than unity, the binary system takes a large number of outer orbits before r_p can diffuse to the small scale of r_t . This leads to a large cumulative MBH perturbation on e_b and increases the probability of the triggering of chaotic tides (and to a less degree the

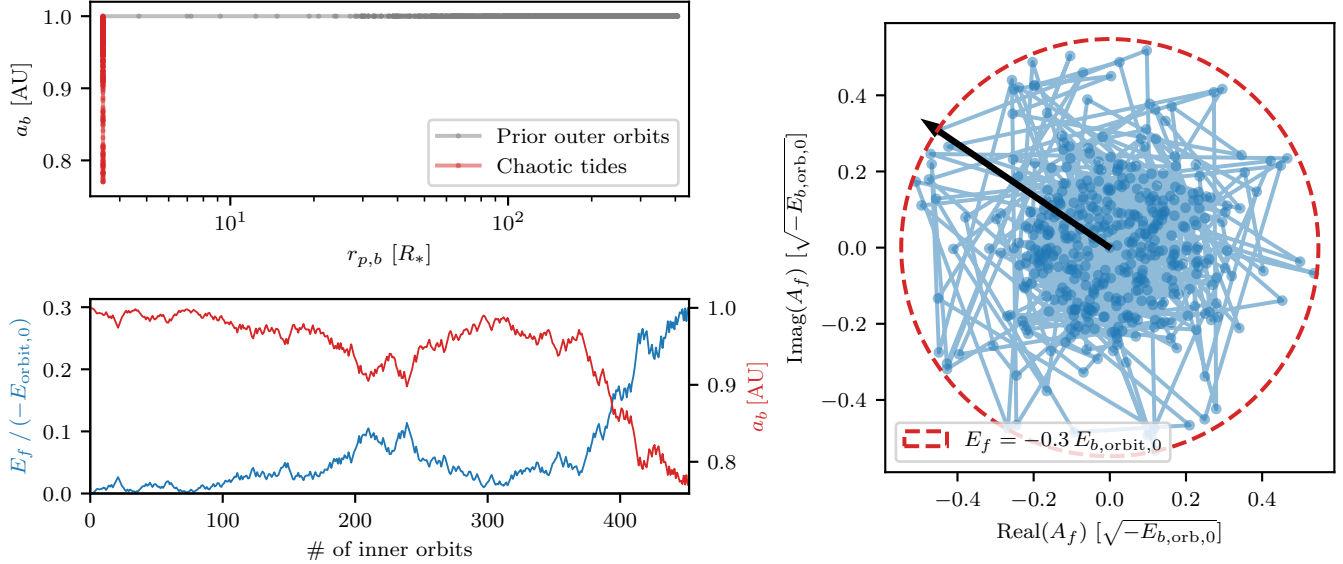


FIG. 6.— A binary system that undergoes chaotic tides. The system has initial conditions $(a, t_{2B,relax}, a_{b,0}, e_{b,0}) = (0.5 \text{ pc}, 1 \text{ Gyr}, 1.0 \text{ AU}, 0.64)$. *Upper left panel:* The evolution of a_b and $r_{p,b}$ over the multiple outer orbits (gray line) and over the final outer orbit when chaotic tides are triggered (red line). The dots indicate the values before each outer/inner pericenter passage. *Lower left panel:* The evolution of E_f (blue line, left axis) and a_b (red line, right axis) over multiple inner orbits after the final outer pericenter passage. *Right panel:* The evolution of the complex amplitude A_f during the growth of chaotic tides. The axis scales are normalized such that $|A_f| = 1$ corresponds to the initial inner orbital binding energy $|E_{b,orbit,0}|$. The red dashed circle marks our criterion for the trigger of the chaotic tides, $E_f = -0.3 \times |E_{b,orbit,0}|$. The black arrow highlights the state of the stellar oscillation at the end of our simulation.

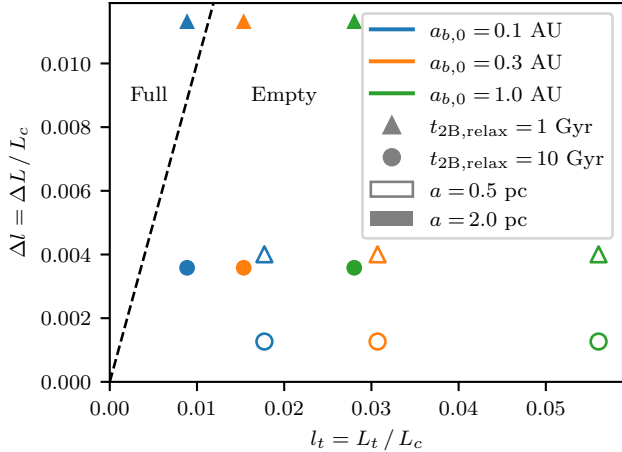


FIG. 7.— The per-outer-orbit angular momentum dispersion Δl versus the angular momentum at the binary disruption radius l_t . Both Δl and l_t (eq. 13) are dimensionless and normalized with $L_c = \sqrt{GM_{\text{BHA}}}a$. The system properties $(a_{b,0}, t_{2B,relax}, a)$ are indicated with different markers. The black dashed line highlights $\Delta l = l_t$, the rough boundary between empty and full loss cone regime.

probability of binary collisions). Since the triggering of chaotic tides requires $r_{p,b} \lesssim r_{b,ct}$, f_{CT} is the highest for $a_{b,0} = 1.0 \text{ AU}$, which has the largest $r_{b,ct}$ and the least stringent requirement for chaotic tides (see Section 2.3). For $a_{b,0} = 0.1 \text{ AU}$, f_{CT} remains low since the triggering of chaotic tides requires the binary to be near contact at the pericenter.

3.3.3. Final pericenter radius

The final outer pericenter radius $r_{p,\text{final}}$ before the binaries reach their end states reflects the nature of the outcomes. Figure 9 shows $r_{p,\text{final}}$ for different binary outcomes as a function of $\Delta l/l_t$ (similar to Figure 8),

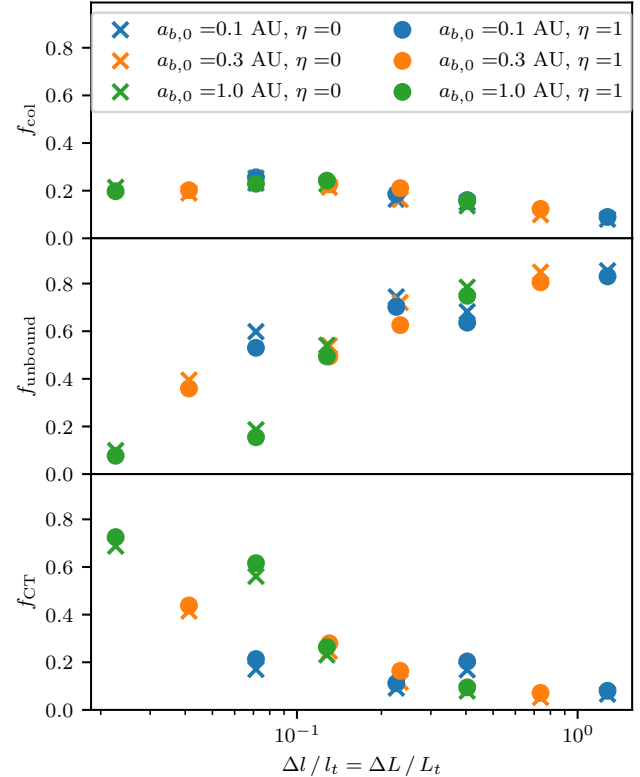


FIG. 8.— The fractions of different outcomes. The top, middle, and bottom panels show the fractions for collision f_{col} , unbound f_{unbound} (Hills breakup), and chaotic tides f_{CT} , respectively. The horizontal axis, $\Delta l/l_t = \Delta L/L_t$ measures the emptiness of the loss cone.

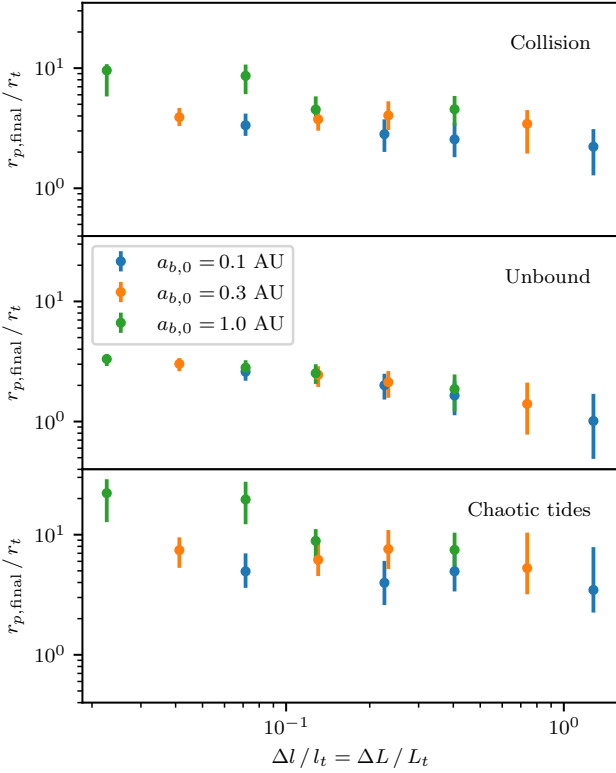


FIG. 9.— The final outer pericenter radius $r_{p,\text{final}}$ for different outcomes. The top, middle, and bottom panels show the cases of collision, unbound (Hills breakup), and chaotic tides, respectively. The horizontal axis, $\Delta l / l_t$ measures the emptiness of the loss cone. For each data point, the center dot is the median value in the simulation, and the error-bar shows the extent of first to third quartiles. Each simulated systems are weighted assuming an initial thermal binary population, with $p(e_{b,0}) \propto e_{b,0}^\eta$ and $\eta = 1$.

assuming a thermal distribution $\eta = 1$. Overall, the Hills breakup happens at the smallest radii $r_{p,\text{final}} \lesssim 3 r_t$, which can be explained by the fact that unbinding the inner orbit requires strong MBH tidal forces that are only achieved for small r_p . Furthermore, $r_{p,\text{final}}$ is smaller in the full loss cone regime ($\Delta l \sim l_t$) than in the full loss cone regime ($\Delta l \ll l_t$). This is because faster relaxation and larger $\Delta l / l_t$ enable the binaries to penetrate deeper into the loss cone. For the chaotic tides outcome, our simulations show that they occur at larger radii than Hills breakup, with $r_{p,\text{final}} \sim 10 r_t$. The larger values of $r_{p,\text{final}}$ for the chaotic tides are because triggering them requires a more gradual MBH perturbation to avoid binary destruction through collision or Hills breakup. Note that $r_{p,\text{final}}$ for $\Delta l / l_b \sim 1$ is not reliable for chaotic tides due to very few such systems in our simulated sample. For binary collisions, $r_{p,\text{final}} \sim 3 - 10 r_t$ is in between those of Hills breakup and chaotic tides.

3.4. Products of Hills breakup

In this subsection we present the statistics of the bound stars and HVS from our REBOUND simulations of the Hills breakup.

3.4.1. Hyper-velocity stars

Ignoring the galactic potential, the HVS ejected by the MBH through the Hills breakup have terminal velocities

v_{HVS} on the order of

$$v_{\text{HVS}} \sim \sqrt{\frac{GM_b}{2a_b}} \left(\frac{M_{\text{BH}}}{M_b} \right)^{1/6}. \quad (16)$$

Figure 10 shows the cumulative distribution functions (CDFs) of v_{HVS} for different $a_{b,0}$. The rare cases where the ejected stars remain bound to the MBH are excluded. Each panel displays a combination of a and $t_{2\text{B},\text{relax}}$, and the statistics are weighted by the thermal distribution of $e_{b,0}$ ($\eta = 1$). The values of v_{HVS} from our REBOUND integrations agree with the analytical estimate (vertical dashed lines; eq. 16), although with a large spread due to variations in the system orientations and $r_{p,\text{final}}$. The size of the spread in v_{HVS} is related to the emptiness of the loss cone. For the empty loss cone cases, all the Hills breakups happen at similar outer pericenter radii, which results in smaller spread in v_{HVS} . For the full loss cone cases, the binary can reach radii much smaller than $3 r_t$, where the stronger MBH tidal forces allow some stars to reach higher v_{HVS} . The second and third panels of Figure 10 represent the empty and (nearly) full loss cones, respectively (see Section 3.3). The CDFs for the full loss cone have longer tails at velocities above the analytical estimate (eq. 16).

One prominent example of HVS of Galactic Center origin is S5-HVS1, which is believed to be a $\approx 2.35 M_\odot$ main-sequence star ejected through the Hills breakup at speed of $v_{\text{ej}} \approx 1800 \text{ km s}^{-1}$ (Koposov *et al.* 2020). If we assume an equal-mass binary with $M_b = 4.7 M_\odot$ and $a_b = 0.3 \text{ AU}$, this ejection speed is about 2.2 times the analytical prediction of 820 km s^{-1} (eq. 16). Given our simulation results (Figure 10), a HVS with v_{HVS} a factor 2 greater than the analytical estimate is rare, and we therefore infer that S5-HVS1 originated from a binary system with $a_b < 0.3 \text{ AU}$ — such a close binary may be primordial or the outcome of chaotic tides in the past.

3.4.2. Stars bound to the MBH

The other star from the Hills breakup remain bound to the MBH on a highly eccentric orbit:

$$1 - e \lesssim \left(\frac{M_b}{M_{\text{BH}}} \right)^{1/3}. \quad (17)$$

Figure 11 shows the orbits of the bound stars from our simulations. The two black lines correspond to $e = 0, 1 - 2(M_b/M_{\text{BH}})^{1/3}$. Most of the bound stars in our simulations have $e > 1 - 2(M_b/M_{\text{BH}})^{1/3} = 0.988$. One constraint on the bound star orbits is the stellar tidal disruption radius:

$$r_{t,*} = R_* \left(\frac{M_{\text{BH}}}{M_*} \right)^{1/3}. \quad (18)$$

Below $r_{t,*}$, the star is destroyed in a TDE, although the exact radius at which this happens depends on the stellar density profile (see e.g., Guillochon and Ramirez-Ruiz 2013; Ryu *et al.* 2020). This inaccessible region of the orbital properties for the bound stars is marked in gray.

In Figure 11 the known S-stars at the galactic center are plotted in gray star markers (Gillessen *et al.* 2017). The low eccentricity of S-stars necessitates additional relaxation processes, if they originate from the

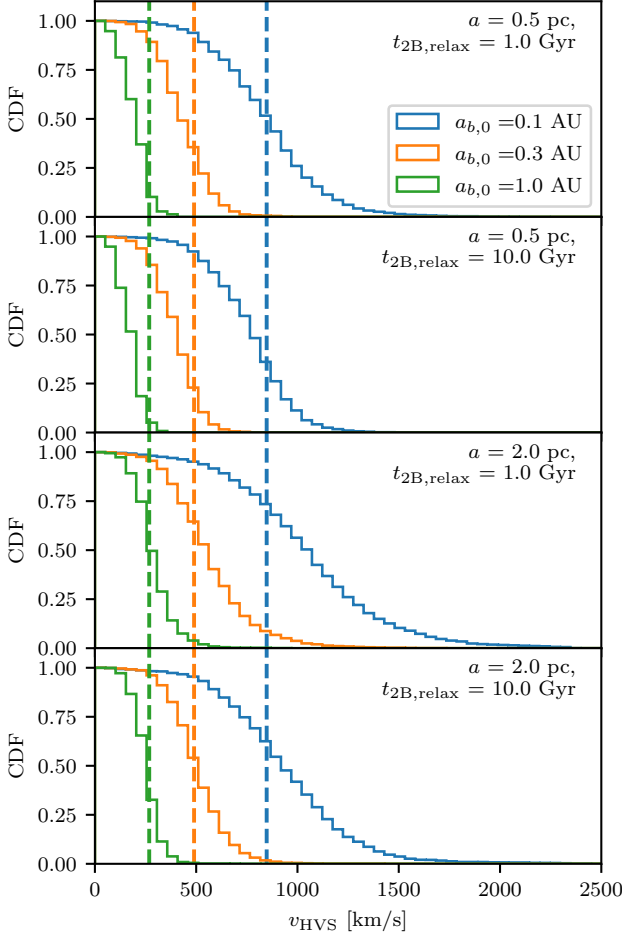


FIG. 10.— The cumulative distribution functions (CDFs) of v_{HVS} from the Hills breakup. Each panel shows the result for a pair of a and $t_{2\text{B,relax}}$, whose values are labeled on the top right corner. The CDFs are constructed by weighting each simulated system with the thermal distribution of $e_{b,0}$ ($\eta = 1$). Note that v_{HVS} only considers the MBH potential and does not include the effects of the galactic potential. The vertical dash lines mark the analytical estimate given by eq. (16).

Hills breakup (Perets *et al.* 2009). There are two main mechanisms to change the bound stars orbit - gravitational wave (GW) orbital decay and the gravitational relaxation. The GW orbital decay shrinks the SMA on the timescale (Peters 1964; Sari and Fragione 2019)

$$t_{\text{GW}} \sim \frac{r_s}{c} \frac{M_{\text{BH}}}{M_*} \left(\frac{r_p}{r_s} \right)^4 \left(\frac{a}{r_p} \right)^{1/2}, \quad (19)$$

where $r_s = 2GM_{\text{BH}}/c^2$ is the Schwarzschild radius. The GW emission and gravitational relaxation modify the highly eccentric orbits in different ways - while GW emission shrinks the SMA and keeps the pericenter radius roughly fixed, the relaxation mainly perturbs the angular momentum and the pericenter radius (see Section 2.1). With only GW orbital decay, the bound stars can be circularized and form the extreme mass ratio inspiral (EMRI). On the contrary, with only the relaxation, the bound stars cannot be circularized and may become TDEs or S-stars (Sari and Fragione 2019; Perets *et al.* 2009). The boundary of $t_{\text{GW}} = t_{L,\text{relax}}$ separates the

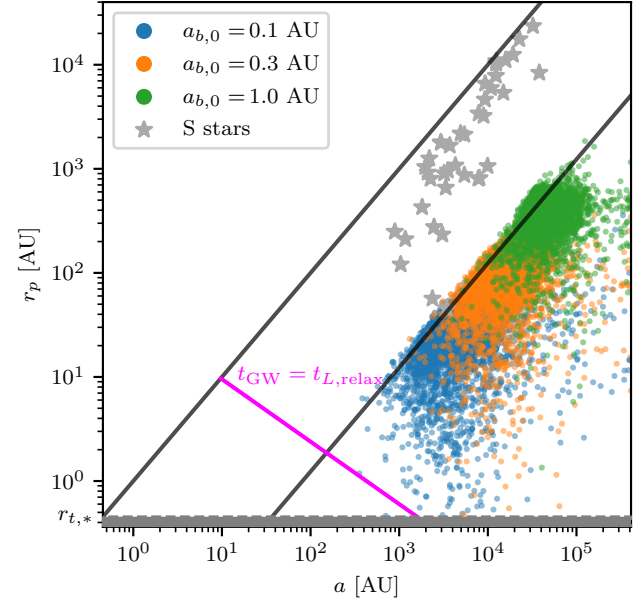


FIG. 11.— The orbital properties of the bound stars after the Hills breakup. The black lines show the constant eccentricity $e = 1, 1 - 2(M_b/M_{\text{BH}})^{1/3}$. The bottom shaded region is where a single star will get tidally disrupted. The orbits of known S-stars are shown in gray star markers. The magenta line marks rough boundary between the dominance of GW emission/relaxation, assuming $t_{2\text{B,relax}} = 1$ Gyr (see eq. 20). Note that in this figure the data from different $a, t_{2\text{B,relax}}$ are combined, and that the distribution of bound stars should not be inspected too closely.

regions in which these two processes dominates:

$$\begin{aligned} \frac{r_p}{r_s} &\sim \left(2t_{2\text{B,relax}} \frac{M_*}{M_{\text{BH}}} \frac{c}{r_s} \right) \left(\frac{a}{r_s} \right)^{-3/5} \\ &\sim 2.0 \times 10^3 \left(\frac{a}{r_s} \right)^{-3/5} \\ &\times \left(\frac{t_{2\text{B,relax}}}{10^9 \text{ yr}} \right)^{2/5} \left(\frac{M_*}{0.5 M_\odot} \right)^{2/5} \left(\frac{M_{\text{BH}}}{4.26 \times 10^6 M_\odot} \right)^{-7/5}. \end{aligned} \quad (20)$$

This boundary is shown in Figure 11 as a magenta line, with $t_{2\text{B,relax}} = 1$ Gyr.⁴ As most of the bound orbits in our simulation are above this boundary and have $t_{\text{GW}} > t_{L,\text{relax}}$, their orbits are mainly affected by relaxation (which changes r_p) and are unlikely to become EMRI. The production of EMRI requires the Hills breakup of tighter binaries with $a_b < 0.1$ AU.

3.5. Collision velocity

For binary collisions, both the radial and tangential velocities, v_r and v_t , at the moment of impact are tracked. The left panel of Figure 12 shows v_t and v_r for all collided systems. The black line highlights $v_r^2 + v_t^2 = v_{\text{esc}}^2$, where $v_{\text{esc}} = \sqrt{2GM_*/R_*}$ is the escape velocity at the radius $r = R_{*,1} + R_{*,2} = 2R_*$. Most of the systems lie on

⁴ In reality, $t_{2\text{B,relax}}$ may weakly depends on the radius r ($t_{2\text{B,relax}} \propto r^{-1/4}$ for a Bahcall-Wolf cusp (Bahcall and Wolf 1976)). This dependence is ignored in our approximation, which makes our boundary slightly different from Sari and Fragione (2019).

this line (as $a_b \gg 2 R_*$) and the collision speed is roughly given by

$$v^2 = \frac{2GM_*}{R_*} \left(1 - \frac{R_*}{a_b}\right) \approx \frac{2GM_*}{R_*}. \quad (21)$$

Our results are similar to that obtained by [Yu and Lai \(2024\)](#). The right panels of Figure 12 further show the cumulative distribution of v_r , assuming a thermal distribution $\eta = 1$. Binary collisions occur at a wide range of angles, from nearly radial ($v_r \sim v_{\text{esc}}$) to tangential ($v_r \sim 0$). The dependence of the v_r distribution on $a_{b,0}$ is weak, except when the loss cone is empty. In the most empty loss cone regime ($t_{2\text{B,relax}} = 10 \text{ Gyr}$, $a = 0.5 \text{ pc}$), the collisions are slightly more tangential for large $a_{b,0}$ (see Figure 7).

4. DISCUSSION

In this section, we examine the assumptions in our simulations and discuss the broader implications of our results. We first review our use of single oscillation mode (f -mode) in modeling the chaotic tides. We then discuss the subsequent consequences of the chaotic tide triggers, including hardening of the inner orbits and the fate of the hardened binaries. Finally, we briefly address the influence of fly-by encounters of field stars on the inner orbits, which is not included in our model.

4.1. Use of single oscillation mode

In our model we only consider the tidal coupling of $l = m = 2$ f -mode in Star 1 to the inner orbit. Our choice of single oscillation mode is conservative, since the inclusion of other oscillation modes will boost the energy exchange and cause a larger change in the inner orbital period. To estimate the potential modifications from including other oscillation modes, we compute the initial energy kick during the first inner pericenter passage by summing up the energy deposition in Star 1 in all the modes with $l \leq 4$ and $0.1 < \omega_\alpha / \sqrt{GM_*/R_*^3} < 20$:

$$\Delta E_{\text{all modes}} = \sum_{\alpha} \Delta E_{\alpha} = \sum_{\alpha} (\Delta A_{\alpha})^2, \quad (22)$$

where α represents each oscillation mode. Figure 13 shows ΔE_f and $\Delta E_{\text{all modes}}$ as functions of $r_{p,b}$ for $a_b = 0.1, 0.3, 1.0 \text{ AU}$. For a given a_b , the contribution of ΔE_f -mode to $\Delta E_{\text{all modes}}$ becomes more and more dominant as $r_{p,b}$ decreases. This is the consequence of two factors: (1) the large tidal overlap integral Q_{α} of $l = m = 2$ f -mode and (2) the orbital angular frequency near the inner pericenter passage $\Omega_{p,b}$ approaches ω_f for small $r_{p,b}$. For large $r_{p,b}$, the g -modes with lower frequencies can couple to the tidal potential more strongly, and the contribution of the f -mode drops. For $r_{p,b} = r_{b,\text{ct}}$, the rough pericenter radius where the chaotic growth of f -mode is triggered (vertical lines in Figure 13), the contribution of ΔE_f to $\Delta E_{\text{all modes}}$ is $\approx 60, 40, 10\%$ for $a_b = 0.1, 0.3, 1.0 \text{ AU}$. Including other oscillation modes will boost energy exchange and increase f_{CT} . Nonetheless, the steep dependence of both ΔE_f -mode and $\Delta E_{\text{all modes}}$ on $r_{p,b}$ suggests that a significant change in the outcome statistics is unlikely.

4.2. Quenching of chaotic tides

After the triggering of chaotic tides, the f -mode energy will grow rapidly and the inner orbit hardens. The growth of the chaotic tides, however, is not indefinite and is instead limited by two factors: (1) the ability of mode-orbit coupling to sustain significant phase change between adjacent orbits, and (2) the damping of f -mode energy.

We first consider the idealized system without mode damping and that the kick amplitude remains the same as that in the first pericenter passage (for simplicity). The f -mode energy evolves with the number of inner orbits k as ([Kochanek 1992](#)):

$$E_{f,k+1} \sim E_{f,k} + 2 \cos \theta \sqrt{E_{f,k} \Delta E_{f,0}} + \Delta E_{f,0}, \quad (23)$$

where θ is the phase difference between the kick and the existing mode. During chaotic tide evolution, the value of θ can be treated as a uniform random variable in the range $(0, 2\pi)$. Sustaining chaotic tides requires a phase change that is greater than unity:

$$1 < \Delta \phi_k = \omega_f (P_{b,k+1} - P_{b,k}) = \frac{3}{2} \left| \frac{E_{f,k+1} - E_{f,k}}{E_{b,\text{orb},k}} \right| \omega_f P_{b,k}. \quad (24)$$

If a significant amount of energy is already present in the f -mode ($E_{f,k} \approx |E_{b,\text{orb},k}| \gg |E_{b,\text{orb},0}|$), the maximum phase change per orbit is:

$$\begin{aligned} \max(\Delta \phi_k) &\approx 3 \left| \frac{\sqrt{E_{f,k} \Delta E_{f,0}}}{E_{b,\text{orb},k}} \right| = 3 \sqrt{\left| \frac{\Delta E_{f,0}}{E_{b,\text{orb},k}} \right|} \omega_f P_{b,k} \\ &= 3 \sqrt{\left| \frac{\Delta E_{f,0}}{E_{b,\text{orb},0}} \right|} \omega_f P_{b,0} \left(\frac{a_{b,k}}{a_{b,0}} \right)^2. \end{aligned} \quad (25)$$

We conservatively assume that the chaotic tides are initially triggered marginally, with

$$1 = \Delta \phi_0 = \frac{3}{2} \left| \frac{\Delta E_{f,0}}{E_{b,\text{orb},0}} \right| \omega_f P_{b,0}. \quad (26)$$

The final SMA at the end of chaotic tides $a_{b,\text{final}}$ is determined by setting $\max(\Delta \phi_k)$ to 1 rad:

$$a_{b,\text{final}} = a_{b,0} (6\omega_f P_{b,0})^{-1/4} \propto a_{b,0}^{5/8}, \quad (27)$$

which is shown by the dotted line in Figure 14.

We next consider the more realistic case where the f -mode is non-linearly damped when it reaches high amplitudes. The non-linear damping timescale in a convective star has been computed by ([Kumar and Goodman 1996](#)):

$$t_{\text{damp}} = t_{\text{damp},0} \left(\frac{E_f}{10^{42} \text{ erg}} \right)^{-1}, \quad (28)$$

where $t_{\text{damp},0}$ is estimated to be around 3×10^4 days. Here we treat it as a variable parameter to account for the fact that the calculations in ([Kumar and Goodman 1996](#)) are based on the solar model, not the $0.5 M_{\odot}$ binary stars in our simulations. The incorporation of damping modifies the energy iterative map ([Kochanek 1992](#)):

$$\begin{aligned} E_{f,k+1} &= E_{f,k} \exp[-P_{b,k}/t_{\text{damp}}(E_{f,k})] + \Delta E_{f,0} \\ &+ 2 \cos \theta \sqrt{E_{f,k} \Delta E_{f,0}} \exp[-P_{b,k}/2t_{\text{damp}}(E_{f,k})]. \end{aligned} \quad (29)$$

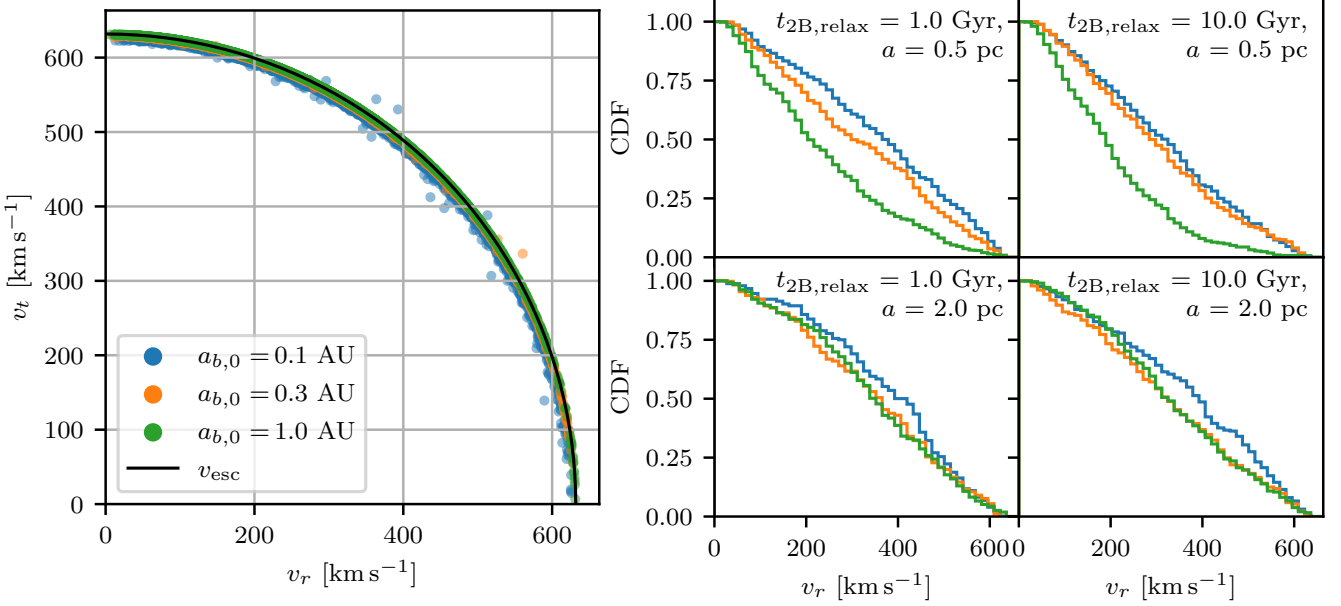


FIG. 12.— The collision velocity of the binaries. *Left panel*: The tangential versus radial collision velocity (v_t vs. v_r). The escape velocity v_{esc} is highlighted with the black line. *Right panel*: The CDF of v_r assuming the thermal distribution of e_b ($\eta = 1$). The four cases correspond to different $t_{2B,\text{relax}}$ and a .

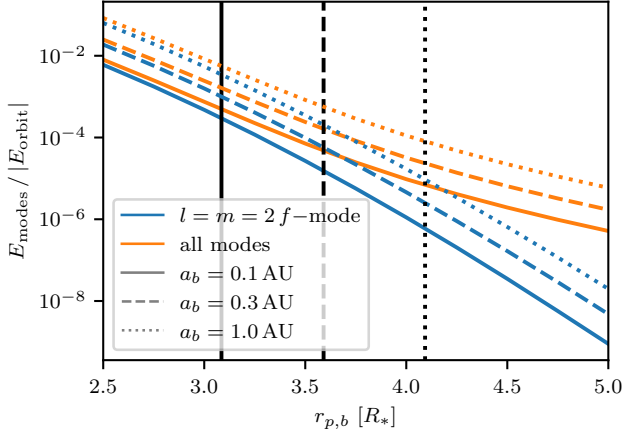


FIG. 13.— The initial energy gain per inner pericenter passage for only the $l = m = 2$ f -mode (blue lines) and all modes (orange lines). The vertical lines show $r_{b,\text{ct}}$ (eq. 9). The solid, dashed, dotted lines are for inner SMAs $a_b = 0.1, 0.3, 1.0$ AU.

Given the randomness of θ , we model the average f -mode energy evolution as the following:

$$\langle E_{f,k+1} \rangle = \langle E_{f,k} \rangle \exp[-P_{b,k}/t_{\text{damp}}(\langle E_{f,k} \rangle)] + \Delta E_{f,0}. \quad (30)$$

The above average iterative model has two evolutionary stages. Initially, the damping of tides is negligible and the average tidal energy grows linearly with the number of inner orbits $\langle E_{f,k} \rangle \sim k \Delta E_{f,0}$. At later time, the large mode amplitude causes the damping to become more effective. Eventually $\langle E_{f,k} \rangle$ saturates and the energy kick balances the energy loss from mode damping per inner orbit:

$$\frac{P_{b,k}}{t_{\text{damp}}(\langle E_{f,k} \rangle)} = \frac{\Delta E_{f,0}}{\langle E_{f,k} \rangle}, \quad (31)$$

where we assume that the damping time is long compared to the orbital period, $t_{\text{damp}}(\langle E_{f,k} \rangle) \gg P_{b,k}$. With the damping timescale prescription in eq. (28), the equi-

librium f -mode energy is given by

$$\langle E_{f,k} \rangle = \left[\frac{t_{\text{damp}}(E = \Delta E_{f,0})}{P_{b,k}} \right]^{1/2} \Delta E_{f,0}. \quad (32)$$

Therefore, in the second stage of chaotic tide growth, the tidal energy will not increase linearly with the number of orbits, but at a smaller rate in response to the shortening of the orbital period. Eventually, the chaotic tides will be quenched when the orbital period change between two consecutive orbits is not sufficient to create enough phase shift in the oscillation mode:

$$\begin{aligned} 1 > \max(\Delta\phi_k) &= 3 \left| \frac{\sqrt{\langle E_{f,k} \rangle \Delta E_{f,0}}}{E_{b,\text{orb},k}} \right| \omega_f P_{b,k} \\ &= 3 \left[\frac{t_{\text{damp}}(E_f = \Delta E_{f,0})}{P_{b,0}} \right]^{1/4} \\ &\quad \times \left(\frac{\Delta E_{f,0}}{E_{b,\text{orb},0}} \right) \omega_f P_{b,0} \left(\frac{a_{b,k}}{a_{b,0}} \right)^{17/8}. \end{aligned} \quad (33)$$

Using the minimum energy kick $\Delta E_{f,0}$ (eq. 26), we can obtain $a_{b,\text{final}}$ in the presence of damping:

$$a_{b,\text{final}} \sim a_{b,0} \left[\frac{16 t_{\text{damp}}(E_f = \Delta E_{f,0})}{P_{b,0}} \right]^{-2/17} \propto a_{b,0}^{15/17}. \quad (34)$$

Figure 14 shows the final SMA of the binary system $a_{b,\text{final}}$ when chaotic tides are quenched. Four possible cases of tidal damping are considered: no damping, $t_{\text{damp},0} = 3 \times 10^3, 3 \times 10^4, 3 \times 10^5$ days. In the absence of damping, the chaotic tides have the potential to shrink the inner SMA by a factor of 5–20, depending on $a_{b,0}$. The efficiency of chaotic tides in hardening the inner orbit drops when non-linear damping is present. In the case of very rapid damping ($t_{\text{damp},0} = 3 \times 10^3$ days), the

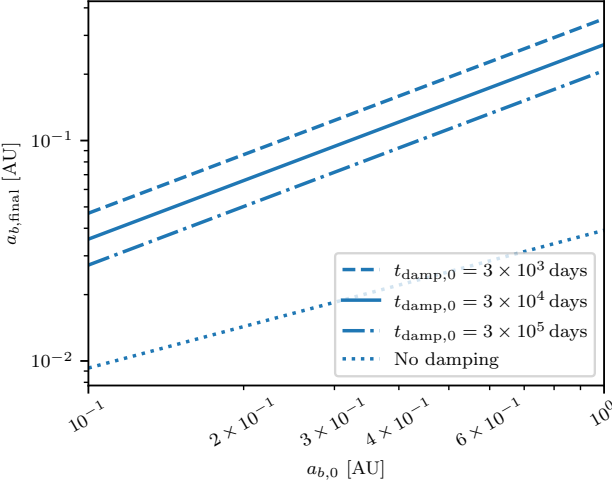


FIG. 14.— The final inner SMA $a_{b,\text{final}}$ at the end of chaotic tides, as the function of the initial inner SMA $a_{b,0}$. The chaotic tides are assumed to be triggered marginally. The dotted line corresponds to the idealized situation without damping (eq. 27). The other lines correspond to the cases where non-linear damping is present (eq. 34). We used the non-linear damping prescription from Kumar and Goodman (1996), with the variable damping time $t_{\text{damp},0}$ (eq. 28).

chaotic tides are only able to shrink the orbit by a factor of 2–3. In general, the chaotic tides have the strongest effect on wide binaries, as $a_{b,\text{final}} / a_{b,0} \propto a_{b,0}^{-2/17}$ (with damping), $\propto a_{b,0}^{-3/8}$ (without damping).

Note that our analysis above does not take into account the potential structural change in the stellar interior during the chaotic tides. The luminosity of energy injected into the star is on the order of

$$L_{\text{ct}} \sim \frac{\Delta E_{f,0}}{P_{b,0}} \gtrsim \frac{|E_{b,\text{orb},0}|}{\omega_f P_{b,0}^2} \sim 10^{33} \left(\frac{a_{b,0}}{1 \text{ AU}} \right)^{-4} \text{ erg s}^{-1}. \quad (35)$$

It is unclear if the star can effectively radiate the energy away. It is possible that the star will expand in radius and the tidal interaction strengthens (Kumar and Goodman 1996), potentially leading to either a runaway or mass loss from the stellar surface.

4.3. Evolution of binaries after chaotic tides

At the end of chaotic tides, the binary systems have $r_{p,b} \sim 2 - 4 R_*$ and $a_b \sim \text{a few} \times 10 R_*$ depending on the initial inner SMA $a_{b,0}$ and the efficiency of non-linear damping (Figure 14). The subsequent evolution of those binaries is governed by two effects: (1) the further circularization of the inner orbits due to the (non-chaotic) tidal interactions between binary stars, and (2) the outer orbit angular momentum relaxation. In this subsection, we discuss the importance of tidal circularization and the final outcome of the binaries.

Studies on the circularization of close binaries have found that dynamical tides can in general provide much more efficient damping compared to equilibrium tides at short periods (Goodman and Dickson 1998; Barker 2020). Those studies mainly concern the systems with small eccentricities and are not directly applicable to binaries at the end of chaotic tides, which still possess significant eccentricity (especially the cases with non-linear damping). In Appendix E, we extrapolate their results

to higher eccentricities based on physical arguments. Despite the great uncertainties associated with the orbital circularization timescale, our estimate suggests that dynamical tides have the potential to harden binaries to $a_b \lesssim 10 R_*$ within one outer orbit, which is much faster than the angular momentum relaxation.

Rapid hardening of binaries leads to a significant shrinkage of r_t , and can save them from the originally imminent Hills breakup. If the binaries later drift away from the MBH due to relaxation, they have the potential to become eclipsing binaries when observed nearly edge-on. On the other hand, if further relaxation brings the hardened binary closer to the MBH and causes it to undergo Hills breakup, the bound star will be delivered on a tighter orbit, with

$$r_p \sim a_b \left(\frac{M_{\text{BH}}}{M_b} \right)^{1/3} \sim 4 \text{ AU} \left(\frac{a_b}{10 R_*} \right), \quad (36)$$

$$a \gtrsim a_b \left(\frac{M_{\text{BH}}}{M_b} \right)^{2/3} \sim 6 \times 10^2 \text{ AU} \left(\frac{a_b}{10 R_*} \right), \quad (37)$$

$$P = 2\pi \sqrt{\frac{a^3}{GM_{\text{BH}}}} \gtrsim 7 \text{ yr} \left(\frac{a_b}{10 R_*} \right)^{3/2}. \quad (38)$$

The steep dependence of t_{GW} on r_p means that the bound stars from those tightest binaries will have the highest chance of avoiding TDE and becoming EMRI through GW circularization (Figure 11):

$$\frac{t_{\text{GW}}}{t_{L,\text{relax}}} \propto r_p^{5/2} a^{3/2} t_{2\text{B},\text{relax}}^{-1} \propto a_b^4. \quad (39)$$

The tight binaries also have the potential to produce the fastest hyper-velocity stars and can explain the high velocity of S5-HVS1 (Koposov *et al.* 2020).

4.4. Influence of other field stars

In our model, we consider the outer orbital relaxation due to the weak gravitational encounters between the binary system and the field stars. In principle, those weak encounters can also influence the inner orbit of binary stars. In the following, we evaluate the significance of those effects and discuss their implications.

For relatively wide binaries ($a_b \geq 0.1 \text{ AU}$), the inner orbital velocities are much smaller than the velocity dispersion in the nuclear star cluster. Over time, the interaction with other field stars tends to increase the inner orbital energy and evaporate the binaries (Heggie 1975). For a binary system surrounded by field stars with velocity dispersion $\sigma \sim \sqrt{GM_{\text{BH}}/r}$ and stellar number density n , the local evaporation timescale is roughly (Binney and Tremaine 2008)

$$t_{\text{evap}}(r) \sim 0.06 \frac{\sigma}{GM_{\odot} n a_b \ln \Lambda}, \quad (40)$$

where we assume field stars of $1 M_{\odot}$ and ignore the order-of-unity dependence on the binary stellar mass. The Coulomb logarithm $\ln \Lambda$ is determined by

$$\ln \Lambda = \ln \left(\frac{a_b/2}{R_*} \right). \quad (41)$$

We take $\ln \Lambda \sim 5$ for our wide binaries ($a_b \sim 0.3 \text{ AU}$). For a power law density profile that is not too steep

$(n \propto r^{-\gamma}; \gamma < 2)$, the interactions near the outer apocenter dominate the contribution to evaporation. Using the stellar mass density $\rho(r) = n(r)M_\odot$ in eq. (A7), t_{evap} is estimated to be:

$$t_{\text{evap}}(r = a) \sim 10^9 \text{ yr} \left(\frac{a}{1 \text{ pc}} \right)^{1.25} \left(\frac{a_b}{0.3 \text{ AU}} \right)^{-1}. \quad (42)$$

This is in general longer than $t_{L,\text{relax}}$ for binaries in our model (eq. 6):

$$t_{L,\text{relax}} \sim 3 \times 10^7 \text{ yr} \left(\frac{a}{1 \text{ pc}} \right)^{-1} \left(\frac{a_b}{0.3 \text{ AU}} \right) \left(\frac{t_{2B,\text{relax}}}{1 \text{ Gyr}} \right). \quad (43)$$

where we use the initial outer pericenter $r_{p,0} = 70 r_t$. The influence of evaporation is therefore limited, except for the widest binaries ($a_b = 1.0 \text{ AU}$) under inefficient relaxation ($t_{2B,\text{relax}} = 10 \text{ Gyr}$).

Another possible outcome of fly-by encounters is the collision between the field stars and the binary system. In general, the collision timescale is not sensitive to the eccentricity of the outer orbit due to gravitational focusing at large radii (Rose *et al.* 2020), and is on the order of (Binney and Tremaine 2008)

$$t_{\text{col}} \sim \frac{1}{16\sqrt{\pi}n\sigma(2R_*)^2} \left(1 + \frac{GM_*/R_*}{4\sigma^2} \right)^{-1}. \quad (44)$$

For $a = 1 \text{ pc}$, $t_{\text{col}} \sim 10^{11} \text{ yr} \gg t_{L,\text{relax}}$ and the collision probability is therefore negligible for our binaries with large outer orbits⁵.

Lastly, the gravitational encounters with field stars can also perturb the inner orbital angular momentum and change e_b . This can happen on a timescale much less than t_{evap} for highly eccentric inner orbits, as the small orbital angular momentum makes the orbit more susceptible to perturbations. Properly evaluating the effects of gravitational encounters on e_b is outside the scope of this paper. However, recently Winter-Granic *et al.* (2024) found that the perturbation on e_b from stellar flybys, combined with the tidal field of the nuclear star cluster, can drive the e_b to extremely high values. This may offer a new venue for triggering the chaotic tides and the formation of hard binaries at the galactic center (e.g., Dodici *et al.* 2025).

5. CONCLUSIONS

In this paper we study the evolution of binary systems orbiting a MBH (taking our own Galactic Center as an example). Our model includes the influence of tidal perturbations from the MBH, gravitational relaxation of the outer orbit, and tidal interactions between the two stars (Figure 1). Our work is motivated by the fact that, unlike the classical Hills mechanism where binary systems approach the MBH and are tidally broken apart in one outer pericenter passage (Hills 1988), the inefficient relaxation (empty loss cone) causes the outer pericenter radius r_p to evolve diffusively, and it takes a large number of outer orbits of relaxation before the binary can reach the disruption radius r_t . During the evolution, the MBH's tides repeatedly perturb the binary's inner

⁵ Note that the effects of collision can be significant for $a \ll 1 \text{ pc}$ (see e.g., Rose *et al.* 2023).

eccentricity e_b . We simulate the perturbation process through analytical prescriptions of secular approximation (Hamers and Samsing 2019) and REBOUND (Rein and Liu 2012; Rein and Spiegel 2015). Our results show that a significant population of binary systems can become highly eccentric, with $r_{p,b} \lesssim \text{a few} \times R_*$, before Hills breakups and stellar collisions. At such small inner pericenter radii, the tidal interactions between binary stars excite the stellar oscillation modes chaotically and lead to a diffusive growth of oscillation amplitudes (Figure 6). Based on analytical arguments and the “iterative map” model (Vick and Lai 2018), we show that the chaotic tides are highly efficient and can harden the binaries within one outer orbit ($\sim 10^5 \text{ yr}$).

Our detailed Monte Carlo simulations further show that the wide binaries ($a_b \sim 1.0 \text{ AU}$) undergoing inefficient outer orbit relaxation ($t_{2B,\text{relax}} \sim 10 \text{ Gyr}$) are the most susceptible to chaotic tides, and up to 50% of the systems that approach the MBH closely can trigger chaotic tides (Figure 8). Even though their subsequent evolution is not modeled in detail, we expect that a combination of non-linear damping of the chaotically excited tides (§4.2) and finite-amplitude dynamical tides (§4.3) can further shrink binaries to $a_b \lesssim 10 R_*$. The evolution of these tight binaries is of great interest. Hills breakup may eject one binary star as an extreme HVS, potentially explaining the high velocity of S5-HVS1 (Koposov *et al.* 2020). On the other hand, the bound companion could evolve into EMRIs through GW orbital decay and produce repeating nuclear transients such as partial TDEs and QPEs (Cufari *et al.* 2022; Payne *et al.* 2021; Miniutti *et al.* 2019; Linial and Sari 2023; Lu and Quataert 2023; Linial and Metzger 2023; Yao and Quataert 2025).

In our model we only consider one stellar oscillation mode ($l = m = 2$ *f*-mode). In principle other oscillation modes also contribute to the tidal interaction, and damping of the dynamical tides of those oscillation modes may help harden the binaries even before the onset of the *f*-mode chaotic tides. Furthermore, gravitational encounters with other field stars may also perturb the inner eccentricity and lead to tidal dissipation (Winter-Granic *et al.* 2024; Dodici *et al.* 2025). Both of these effects may contribute to the formation of close binaries at galactic centers.

In summary, our work extends the traditional picture of Hills breakup to include the long-term evolution of binary systems. Through MBH tidal perturbations and tidal interactions between binary stars, we demonstrate the effectiveness of chaotic tides at hardening the binaries. A significant population of close binaries formed through this mechanism may be present at our own Galactic Center and in the nuclei of other galaxies. Future works on their evolution will be essential to uncovering the connection between such binaries and repeating partial TDEs or QPEs.

ACKNOWLEDGMENTS

We thank Dong Lai for helpful suggestions along this project. The research of HH and WL are supported by Rose Hills Innovator Program. We thank the participants of the ZTF Theory Network meeting at Oak Creek, especially Jim Fuller, Itai Linial, Eliot Quataert, and Sterl Phinney, for many stimulating discussions and this research benefited from interactions supported by

the Gordon and Betty Moore Foundation through Grant GBMF5076. We also thank the organizers (especially Giovanni Miniutti) of the X-ray Quasi-Periodic Eruptions & Repeating Nuclear Transients Conference in Spain where we have received helpful comments on this work.

REFERENCES

W. R. Brown, *ARA&A* **53**, 15 (2015).

J. G. Hills, *Nature* **331**, 687 (1988).

Q. Yu and S. Tremaine, *ApJ* **599**, 1129 (2003), [arXiv:astro-ph/0309084 \[astro-ph\]](https://arxiv.org/abs/astro-ph/0309084).

B. C. Bromley, S. J. Kenyon, M. J. Geller, E. Barcikowski, W. R. Brown, and M. J. Kurtz, *ApJ* **653**, 1194 (2006), [arXiv:astro-ph/0608159 \[astro-ph\]](https://arxiv.org/abs/astro-ph/0608159).

R. Sari, S. Kobayashi, and E. M. Rossi, *ApJ* **708**, 605 (2010), [arXiv:0911.1136 \[astro-ph.HE\]](https://arxiv.org/abs/0911.1136).

E. M. Rossi, S. Kobayashi, and R. Sari, *ApJ* **795**, 125 (2014), [arXiv:1307.1134 \[astro-ph.GA\]](https://arxiv.org/abs/1307.1134).

A. Generozov and A.-M. Madigan, *ApJ* **896**, 137 (2020), [arXiv:2002.10547 \[astro-ph.GA\]](https://arxiv.org/abs/2002.10547).

F. Yu and D. Lai, *ApJ* **977**, 268 (2024), [arXiv:2409.09597 \[astro-ph.HE\]](https://arxiv.org/abs/2409.09597).

B. Sersante, Z. Penoyre, and E. M. Rossi, *MNRAS* (2025), [10.1093/mnras/staf1766](https://doi.org/10.1093/mnras/staf1766), [arXiv:2505.08499 \[astro-ph.GA\]](https://arxiv.org/abs/2505.08499).

B. Bradnick, I. Mandel, and Y. Levin, *MNRAS* **469**, 2042 (2017), [arXiv:1703.05796 \[astro-ph.HE\]](https://arxiv.org/abs/1703.05796).

A. P. Stephan, S. Naoz, A. M. Ghez, M. R. Morris, A. Ciurlo, T. Do, K. Breivik, S. Coughlin, and C. L. Rodriguez, *ApJ* **878**, 58 (2019), [arXiv:1903.00010 \[astro-ph.SR\]](https://arxiv.org/abs/1903.00010).

J. P. Zahn, *A&A* **57**, 383 (1977).

P. Hut, *A&A* **99**, 126 (1981).

P. P. Eggleton, L. G. Kiseleva, and P. Hut, *ApJ* **499**, 853 (1998), [arXiv:astro-ph/9801246 \[astro-ph\]](https://arxiv.org/abs/astro-ph/9801246).

C. S. Kochanek, *ApJ* **385**, 604 (1992).

R. A. Mardling, *ApJ* **450**, 722 (1995).

Y. Wu, *AJ* **155**, 118 (2018), [arXiv:1710.02542 \[astro-ph.EP\]](https://arxiv.org/abs/1710.02542).

M. Vick and D. Lai, *MNRAS* **476**, 482 (2018), [arXiv:1708.09392 \[astro-ph.SR\]](https://arxiv.org/abs/1708.09392).

R. Sari and G. Fragione, *ApJ* **885**, 24 (2019), [arXiv:1907.03312 \[astro-ph.GA\]](https://arxiv.org/abs/1907.03312).

W. Lu, J. Fuller, Y. Raveh, H. B. Perets, T. S. Li, M. W. Hosek, Jr., and T. Do, *MNRAS* **503**, 603 (2021), [arXiv:2005.12300 \[astro-ph.HE\]](https://arxiv.org/abs/2005.12300).

I. Linial and R. Sari, *ApJ* **945**, 86 (2023), [arXiv:2211.09851 \[astro-ph.HE\]](https://arxiv.org/abs/2211.09851).

G. Miniutti, R. D. Saxton, M. Giustini, K. D. Alexander, R. P. Fender, I. Heywood, I. Monageng, M. Coriat, A. K. Tzioumis, A. M. Read, C. Knigge, P. Gandhi, M. L. Pretorius, and B. Agís-González, *Nature* **573**, 381 (2019), [arXiv:1909.04693 \[astro-ph.HE\]](https://arxiv.org/abs/1909.04693).

M. Giustini, G. Miniutti, and R. D. Saxton, *A&A* **636**, L2 (2020), [arXiv:2002.08967 \[astro-ph.HE\]](https://arxiv.org/abs/2002.08967).

R. Arcodia, A. Merloni, K. Nandra, J. Buchner, M. Salvato, D. Pasham, R. Remillard, J. Comparat, G. Lamer, G. Ponti, A. Malyali, J. Wolf, Z. Arzoumanian, D. Bogensberger, D. A. H. Buckley, K. Gendreau, M. Gromadzki, E. Kara, M. Krumpe, C. Markwardt, M. E. Ramos-Ceja, A. Rau, M. Schramm, and A. Schworer, *Nature* **592**, 704 (2021), [arXiv:2104.13388 \[astro-ph.HE\]](https://arxiv.org/abs/2104.13388).

A. V. Payne, B. J. Shappee, J. T. Hinkle, P. J. Valletta, C. S. Kochanek, T. W. S. Holoi, K. Auchettl, K. Z. Stanek, T. A. Thompson, J. M. M. Neustadt, M. A. Tucker, J. D. Armstrong, J. Brimacombe, P. Cacella, R. Corbett, L. Denneau, M. M. Fausnaugh, H. Flewelling, D. Grupe, A. N. Heinze, L. A. Lopez, B. Monard, J. L. Prieto, A. C. Schneider, S. S. Sheppard, J. L. Tonry, and H. Weiland, *ApJ* **910**, 125 (2021), [arXiv:2009.03321 \[astro-ph.HE\]](https://arxiv.org/abs/2009.03321).

M. Cufari, E. R. Coughlin, and C. J. Nixon, *ApJ* **929**, L20 (2022), [arXiv:2203.08162 \[astro-ph.HE\]](https://arxiv.org/abs/2203.08162).

W. Lu and E. Quataert, *MNRAS* **524**, 6247 (2023), [arXiv:2210.08023 \[astro-ph.HE\]](https://arxiv.org/abs/2210.08023).

I. Linial and B. D. Metzger, *ApJ* **957**, 34 (2023), [arXiv:2303.16231 \[astro-ph.HE\]](https://arxiv.org/abs/2303.16231).

P. Z. Yao and E. Quataert, *arXiv e-prints*, [arXiv:2505.10611 \[astro-ph.HE\]](https://arxiv.org/abs/2505.10611).

L. Makrygianni, I. Arcavi, M. Newsome, A. Bandopadhyay, E. R. Coughlin, I. Linial, B. Mockler, E. Quataert, C. Nixon, B. Godson, M. Pursiainen, G. Leloudas, K. D. French, A. Zitrin, S. Faris, M. C. Lam, A. Horesh, I. Sfaradi, M. Fausnaugh, E. Nakar, K. Ackley, M. Andrews, P. Charalampopoulos, B. D. R. Davies, Y. Dgany, M. J. Dyer, J. Farah, R. Fender, D. A. Green, D. A. Howell, T. Killestein, N. Koivisto, J. Lyman, C. McCully, M. A. Mitchell, E. Padilla Gonzalez, L. Rhodes, A. Sahu, G. Terreran, and B. Warwick, *ApJ* **987**, L20 (2025), [arXiv:2505.16867 \[astro-ph.HE\]](https://arxiv.org/abs/2505.16867).

D. Pasham, S. Kejriwal, E. Coughlin, V. Witzany, A. J. K. Chua, M. Zajáček, T. Wevers, and Y. Ajay, *arXiv e-prints*, [arXiv:2411.00289 \[astro-ph.HE\]](https://arxiv.org/abs/2411.00289).

J. Chakraborty, E. Kara, R. Arcodia, J. Buchner, M. Giustini, L. Hernández-García, I. Linial, M. Masterson, G. Miniutti, A. Mummery, C. Panagiotou, E. Quintin, and P. Sánchez-Sáez, *ApJ* **983**, L39 (2025), [arXiv:2503.19013 \[astro-ph.HE\]](https://arxiv.org/abs/2503.19013).

I. Mandel and Y. Levin, *ApJ* **805**, L4 (2015), [arXiv:1504.02787 \[astro-ph.SR\]](https://arxiv.org/abs/1504.02787).

M. Dodici, S. Tremaine, and Y. Wu, *arXiv e-prints*, [arXiv:2511.02905 \[astro-ph.GA\]](https://arxiv.org/abs/2511.02905).

GRAVITY Collaboration, R. Abuter, A. Amorim, M. Bauböck, J. P. Berger, H. Bonnet, W. Brandner, V. Cardoso, Y. Clément, P. T. de Zeeuw, J. Dexter, A. Eckart, F. Eisenhauer, N. M. Förster Schreiber, P. García, F. Gao, E. Gendron, R. Genzel, S. Gillessen, M. Habibi, X. Haubois, T. Henning, S. Hippel, M. Horrobin, A. Jiménez-Rosales, L. Jochum, L. Jocou, A. Kaufer, P. Kervella, S. Lacour, V. Lapeyrère, J. B. Le Bouquin, P. Léna, M. Nowak, T. Ott, T. Paumard, K. Perraut, G. Perrin, O. Pfuhl, G. Rodríguez-Coira, J. Shangguan, S. Scheithauer, J. Stadler, O. Straub, C. Straubmeier, E. Sturm, L. J. Tacconi, F. Vincent, S. von Fellenberg, I. Waisberg, F. Widmann, E. Wieprecht, E. Wiezorrek, J. Woillez, S. Yazici, and G. Zins, *A&A* **636**, L5 (2020), [arXiv:2004.07187 \[astro-ph.GA\]](https://arxiv.org/abs/2004.07187).

W. H. Press and S. A. Teukolsky, *ApJ* **213**, 183 (1977).

A. S. Hamers and J. Samsing, *MNRAS* **487**, 5630 (2019), [arXiv:1904.09624 \[astro-ph.SR\]](https://arxiv.org/abs/1904.09624).

S. Naoz, *ARA&A* **54**, 441 (2016), [arXiv:1601.07175 \[astro-ph.EP\]](https://arxiv.org/abs/1601.07175).

H. Rein and S. F. Liu, *A&A* **537**, A128 (2012), [arXiv:1110.4876 \[astro-ph.EP\]](https://arxiv.org/abs/1110.4876).

H. Rein and D. S. Spiegel, *MNRAS* **446**, 1424 (2015), [arXiv:1409.4779 \[astro-ph.EP\]](https://arxiv.org/abs/1409.4779).

P. P. Eggleton and L. Kiseleva-Eggleton, *ApJ* **562**, 1012 (2001), [arXiv:astro-ph/0104126 \[astro-ph\]](https://arxiv.org/abs/astro-ph/0104126).

B. Paxton, L. Bildsten, A. Dotter, F. Herwig, P. Lesaffre, and F. Timmes, *ApJS* **192**, 3 (2011), [arXiv:1009.1622 \[astro-ph.SR\]](https://arxiv.org/abs/1009.1622).

B. Paxton, M. Cantiello, P. Arras, L. Bildsten, E. F. Brown, A. Dotter, C. Mankovich, M. H. Montgomery, D. Stello, F. X. Timmes, and R. Townsend, *ApJS* **208**, 4 (2013), [arXiv:1301.0319 \[astro-ph.SR\]](https://arxiv.org/abs/1301.0319).

B. Paxton, P. Marchant, J. Schwab, E. B. Bauer, L. Bildsten, M. Cantiello, L. Dessart, R. Farmer, H. Hu, N. Langer, R. H. D. Townsend, D. M. Townsley, and F. X. Timmes, *ApJS* **220**, 15 (2015), [arXiv:1506.03146 \[astro-ph.SR\]](https://arxiv.org/abs/1506.03146).

B. Paxton, J. Schwab, E. B. Bauer, L. Bildsten, S. Blinnikov, P. Duffell, R. Farmer, J. A. Goldberg, P. Marchant, E. Sorokina, A. Thoul, R. H. D. Townsend, and F. X. Timmes, *ApJS* **234**, 34 (2018), [arXiv:1710.08424 \[astro-ph.SR\]](https://arxiv.org/abs/1710.08424).

B. Paxton, R. Smolec, J. Schwab, A. Gautschi, L. Bildsten, M. Cantiello, A. Dotter, R. Farmer, J. A. Goldberg, A. S. Jermyn, S. M. Kanbur, P. Marchant, A. Thoul, R. H. D. Townsend, W. M. Wolf, M. Zhang, and F. X. Timmes, *ApJS* **243**, 10 (2019), [arXiv:1903.01426 \[astro-ph.SR\]](https://arxiv.org/abs/1903.01426).

A. S. Jermyn, E. B. Bauer, J. Schwab, R. Farmer, W. H. Ball, E. P. Bellinger, A. Dotter, M. Joyce, P. Marchant, J. S. G. Mombarg, W. M. Wolf, T. L. Sunny Wong, G. C. Cinquegrana, E. Farrell, R. Smolec, A. Thoul, M. Cantiello, F. Herwig, O. Toloza, L. Bildsten, R. H. D. Townsend, and F. X. Timmes, *ApJS* **265**, 15 (2023), [arXiv:2208.03651 \[astro-ph.SR\]](https://arxiv.org/abs/2208.03651).

R. H. D. Townsend and S. A. Teitler, *MNRAS* **435**, 3406 (2013), [arXiv:1308.2965 \[astro-ph.SR\]](#).

F. Zhang, Y. Lu, and Q. Yu, *ApJ* **722**, 1744 (2010), [arXiv:1105.1432 \[astro-ph.GA\]](#).

S. E. Koposov, D. Boubert, T. S. Li, D. Erkal, G. S. Da Costa, D. B. Zucker, A. P. Ji, K. Kuehn, G. F. Lewis, D. Mackey, J. D. Simpson, N. Shipp, Z. Wan, V. Belokurov, J. Bland-Hawthorn, S. L. Martell, T. Nordlander, A. B. Pace, G. M. De Silva, M.-Y. Wang, and S5 Collaboration, *MNRAS* **491**, 2465 (2020), [arXiv:1907.11725 \[astro-ph.GA\]](#).

J. Guillen and E. Ramirez-Ruiz, *ApJ* **767**, 25 (2013), [arXiv:1206.2350 \[astro-ph.HE\]](#).

T. Ryu, J. Krolik, T. Piran, and S. C. Noble, *ApJ* **904**, 99 (2020), [arXiv:2001.03502 \[astro-ph.HE\]](#).

S. Gillessen, P. M. Plewa, F. Eisenhauer, R. Sari, I. Waisberg, M. Habibi, O. Pfuhl, E. George, J. Dexter, S. von Fellenberg, T. Ott, and R. Genzel, *ApJ* **837**, 30 (2017), [arXiv:1611.09144 \[astro-ph.GA\]](#).

H. B. Perets, A. Gualandris, G. Kupi, D. Merritt, and T. Alexander, *ApJ* **702**, 884 (2009), [arXiv:0903.2912 \[astro-ph.GA\]](#).

P. C. Peters, *Physical Review* **136**, 1224 (1964).

J. N. Bahcall and R. A. Wolf, *ApJ* **209**, 214 (1976).

P. Kumar and J. Goodman, *ApJ* **466**, 946 (1996), [arXiv:astro-ph/9509112 \[astro-ph\]](#).

J. Goodman and E. S. Dickson, *ApJ* **507**, 938 (1998), [arXiv:astro-ph/9801289 \[astro-ph\]](#).

A. J. Barker, *MNRAS* **498**, 2270 (2020), [arXiv:2008.03262 \[astro-ph.EP\]](#).

D. C. Heggie, *MNRAS* **173**, 729 (1975).

J. Binney and S. Tremaine, *Galactic Dynamics: Second Edition* (2008).

S. C. Rose, S. Naoz, A. K. Gautam, A. M. Ghez, T. Do, D. Chu, and E. Becklin, *ApJ* **904**, 113 (2020), [arXiv:2008.06512 \[astro-ph.SR\]](#).

S. C. Rose, S. Naoz, R. Sari, and I. Linial, *ApJ* **955**, 30 (2023), [arXiv:2304.10569 \[astro-ph.GA\]](#).

M. Winter-Granic, C. Petrovich, V. Peña-Donaire, and C. Hamilton, *ApJ* **973**, 53 (2024), [arXiv:2312.17319 \[astro-ph.GA\]](#).

D. C. Heggie and F. A. Rasio, *MNRAS* **282**, 1064 (1996), [arXiv:astro-ph/9506082 \[astro-ph\]](#).

D. Merritt, *Dynamics and Evolution of Galactic Nuclei* (2013).

R. Schödel, A. Eckart, T. Alexander, D. Merritt, R. Genzel, A. Sternberg, L. Meyer, F. Kul, J. Moutata, T. Ott, and C. Straubmeier, *A&A* **469**, 125 (2007), [arXiv:astro-ph/0703178 \[astro-ph\]](#).

P. B. Ivanov and J. C. B. Papaloizou, *MNRAS* **347**, 437 (2004), [arXiv:astro-ph/0303669 \[astro-ph\]](#).

A. K. Schenk, P. Arras, É. Flanagan, S. A. Teukolsky, and I. Wasserman, *Phys. Rev. D* **65**, 024001 (2001), [arXiv:gr-qc/0101092 \[gr-qc\]](#).

J. Burkart, E. Quataert, P. Arras, and N. N. Weinberg, *MNRAS* **421**, 983 (2012), [arXiv:1108.3822 \[astro-ph.SR\]](#).

J. Fuller, *MNRAS* **472**, 1538 (2017), [arXiv:1706.05054 \[astro-ph.SR\]](#).

D. Lai, *ApJ* **490**, 847 (1997), [arXiv:astro-ph/9704132 \[astro-ph\]](#).

APPENDIX

PRECESSIONS OF THE INNER AND OUTER ORBITS

There are several precession mechanisms in the MBH-binary system, the leading-order ones being the Schwarzschild precession of the inner and outer orbits, and the mass precession of the outer orbit. The precessions mainly affect the relative orientation between the inner and outer orbits, and influence the MBH perturbation on the binary (Section 2.2). In this subsection we evaluate the importance of those precessions in our modeling.

Schwarzschild precession of inner/outer orbits

The Schwarzschild precession per inner orbit is given by

$$\Delta\omega_{s,\text{inner}} = \frac{6\pi GM_b}{c^2 a_b (1 - e_b^2)}. \quad (\text{A1})$$

Since $r_{p,b} \gtrsim r_{b,\text{ct}}$ before the chaotic tides, $\Delta\omega_{s,\text{inner}}$ is limited by:

$$\Delta\omega_{s,\text{inner}} \lesssim \frac{3\pi GM_b}{c^2 r_{b,\text{ct}}} \simeq 1 \times 10^{-5} \left(\frac{r_{b,\text{ct}}}{4R_*} \right)^{-1}. \quad (\text{A2})$$

Despite the small value of $\Delta\omega_{s,\text{inner}}$, the cumulative inner orbital Schwarzschild precession over one outer orbit can be significant:

$$\begin{aligned} \Delta\omega_{s,\text{inner,tot}} &= \Delta\omega_{s,\text{inner}} \left(\frac{P}{P_b} \right) \\ &\lesssim 0.48 \left(\frac{a}{1\text{pc}} \right)^{3/2} \left(\frac{a_b}{1\text{AU}} \right)^{-3/2} \left(\frac{r_{b,\text{ct}}}{4R_*} \right)^{-1}. \end{aligned} \quad (\text{A3})$$

The inner orbit Schwarzschild precession directly changes the result of each MBH perturbation, which can be seen

from the first-order perturbation theory (Heggie and Rasio 1996). We include the inner orbit Schwarzschild precession in our model by adding $\Delta\omega_{s,\text{inner,tot}}$ to the inner argument of pericenter before the MBH perturbation every outer orbit.

While the outer orbit also undergoes Schwarzschild precession, it is much weaker:

$$\Delta\omega_{s,\text{outer}} \approx \frac{3\pi GM_{\text{BH}}}{c^2 r_p} = 3.6 \times 10^{-5} \left(\frac{r_p}{70r_t} \right)^{-1} \left(\frac{a_b}{1\text{AU}} \right)^{-1}. \quad (\text{A4})$$

More specifically, the outer orbital Schwarzschild precession is slow compared to the angular momentum relaxation

$$\begin{aligned} \Delta\omega_{s,\text{outer}} N_l &\approx \frac{6\pi GM_{\text{BH}}}{c^2 a} \frac{t_{2\text{B,relax}}}{P(a)} \\ &= 0.08 \left(\frac{t_{2\text{B,relax}}}{1\text{Gyr}} \right) \left(\frac{a}{1\text{pc}} \right)^{-5/2}. \end{aligned} \quad (\text{A5})$$

Since the orientation of the outer orbit is expected to change significantly due to mass precession (see below) even without the Schwarzschild precession, $\Delta\omega_{s,\text{outer}}$ is unimportant and hence not included in our model.

Mass precession of outer orbit

Due to the extended distribution of the stellar/compact object population near the MBH, the outer orbit is subject to the mass precession. Ignoring the order-of-unity correction from the density profile, the mass precession per outer orbit is given by (Merritt 2013)

$$\Delta\omega_{\text{mass}} \sim -2\pi\sqrt{1-e^2} \frac{M(a)}{M_{\text{BH}}} \sim -2\pi\sqrt{\frac{2r_p}{a}} \frac{M(a)}{M_{\text{BH}}}, \quad (\text{A6})$$

where $M(a)$ is the extended mass within radius a from the MBH. We use the density profile from Schödel *et al.*

(2007)

$$\rho(r) = 2.8 \times 10^6 M_{\odot} \text{ pc}^{-3} \times \left(\frac{r}{0.22 \text{ pc}} \right)^{-\gamma}, \quad (\text{A7})$$

where $\gamma = 1.2$ for $r < 0.22 \text{ pc}$ and $\gamma = 1.75$ for $r > 0.22 \text{ pc}$. The corresponding $M(r)$ for $r > 0.22 \text{ pc}$ is

$$M(r) = 3.0 \times 10^5 M_{\odot} \left(\frac{r}{0.22 \text{ pc}} \right)^{1.25} - 9 \times 10^4 M_{\odot}. \quad (\text{A8})$$

For a binary system with $a_b = 70 r_t$ and $a = 1.0 \text{ pc}$, $M(r = a) \sim 2 \times 10^6 M_{\odot}$ and $\Delta\omega_{\text{mass}} \sim -1 \text{ rad}$. Even though the mass precession does not directly affect the MBH perturbation on the binary, its indirectly influence orientation and the relaxation of the outer orbit. In our model, the mass precession is included by adding $\Delta\omega_{\text{mass}}$ to the outer argument of pericenter before the MBH perturbation every outer orbit.

METHOD OF ITERATIVE MAP

(In this section the subscript b is omitted, and all orbital properties refer to the inner orbit.)

The iterative map concerns the stellar/planet oscillation mode evolution in highly eccentric binary systems. It was first introduced by [Ivanov and Papaloizou \(2004\)](#) and further developed by [Vick and Lai \(2018\)](#). Here we briefly summarize [Vick and Lai \(2018\)](#)'s approach. For a non-rotating star (Star 1), the general first-order Lagrangian displacement of the fluid elements $\xi(\mathbf{x}, t)$ can be expanded with the eigenmodes α with eigenfunctions $\xi_{\alpha}(\mathbf{x})$ and eigenfrequencies ω_{α} ([Schenk et al. 2001](#)):

$$\left[\frac{\partial \xi(\mathbf{x}, t)}{\partial t} \right] = \sum_{\alpha} c_{\alpha}(t) \begin{bmatrix} \xi_{\alpha}(\mathbf{x}) \\ -i\omega_{\alpha} \xi_{\alpha}(\mathbf{x}) \end{bmatrix}. \quad (\text{B1})$$

The eigenfunctions are normalized with $\int_V \rho \xi_{\alpha}^* \cdot \xi_{\alpha} d^3x = 1$. In the presence of an external tidal potential from the companion (Star 2), the coefficients c_{α} evolve according to

$$\dot{c}_{\alpha} + i\omega_{\alpha} c_{\alpha} = \frac{i}{2\omega_{\alpha}} \frac{GM_{b,2}}{r(t)^{l+1}} W_{lm} Q_{\alpha} e^{-im\Phi(t)}, \quad (\text{B2})$$

where $r(t)$ is the binary separation and $\Phi(t)$ is the true anomaly of the orbit. The damping is ignored in the above expression. W_{lm} is a numerical constant and Q_{α} is the tidal overlap integral that depends on the spatial structure of the oscillation modes ([Press and Teukolsky 1977](#)):

$$Q_{\alpha} = \int_V \rho \xi_{\alpha}^* \cdot \nabla (r^l Y_{lm}) d^3x, \quad (\text{B3})$$

where ρ is the stellar density profile prior to perturbation and Y_{lm} is the spherical harmonics corresponding to the mode α . Another equivalent expression of Q_{α} is ([Burkart et al. 2012; Fuller 2017](#))

$$Q_{\alpha} = -(2l+1) \frac{R_{*,1}^{l+1}}{4\pi G} \tilde{\Phi}_{\alpha}(R_{*,1}), \quad (\text{B4})$$

where $\tilde{\Phi}_{\alpha}(R_{*,1})$ is the Eulerian gravitational potential perturbation on the surface of the star. We further define

the dimensionless tidal overlap integral \bar{Q}_{α} :

$$\bar{Q}_{\alpha} = \frac{Q_{\alpha}}{M_{*,1}^{1/2} R_{*,1}^{l-1}}. \quad (\text{B5})$$

While in principle eq. (B2) can be combined with the back reaction of the oscillation on the orbital dynamics to solve the tidal evolution of the binary system ([Wu 2018](#)), the drastically different timescales between orbital dynamics and stellar oscillations make numerical integrations very challenging. Iterative maps utilize the fact that in highly eccentric orbits, the tidal interaction and driving of oscillation modes are limited to the region near pericenter. By approximating the orbits between consecutive pericenter passages as ellipses, the stellar oscillations can be solved iteratively over multiple orbits. We focus on the iterative map of only $l = m = 2$ f -mode, which dominates the oscillation energy in a highly eccentric binary of low mass stars (see Section 4.1). For $0.5 M_{\odot}$ ZAMS stars, this mode has $\omega_f/\Omega_{*,1} = 1.67084$ and $\bar{Q}_f = 0.1198$ based on MESA and GYRE calculations. Here $\Omega_{*,1} = \sqrt{GM_{*,1}/R_{*,1}^3}$ is the angular frequency associated with the dynamical time of Star 1.

Let t_k be the time of k -th apocenter passage, $t_{k+1/2}$ be the time of k -th pericenter passage, and $c_{f,k} = c_f(t_k)$. Define a new variable $A_{f,k}$ to represent the amplitude of the oscillation modes:

$$A_{f,k} = \sqrt{2\omega_f} c_{f,k} e^{-i\omega_f P_k/2}, \quad (\text{B6})$$

where $P_k = t_{k+1/2} - t_{k-1/2}$ is the period of the k -th inner orbit. The energy and angular momentum in the mode are $E_{f,k} = |A_{f,k}|^2$, $L_{f,k} = m |A_{f,k}|^2 / \omega_f$. The evolution of $A_{f,k}$ follows the iterative map below:

$$A_{f,k+1} = (A_{f,k+1} + \Delta A_{f,k}) e^{i\omega_f P_{k+1}}. \quad (\text{B7})$$

The energy transfer due to the tidal interaction during the pericenter passage is encapsulated in ΔA_k :

$$\Delta A_{f,k} = \frac{i\sqrt{2\pi} GM_{*,2} Q_f}{r_{p,k}^{l+1}} \frac{1}{\Omega_{*,1}} K_{f,k}, \quad (\text{B8})$$

where $r_{p,k}$ is the k -th pericenter radius, and $K_{f,k}$ is an integral that quantifies the temporal coupling between the oscillation mode and the tidal potential. In general, K_f depends on ω_f and orbital parameters:

$$K_f = \frac{W_{lm}}{2\pi} \Omega_{*,1} \int_{-P/2}^{P/2} \left[\frac{r_p}{r(t)} \right]^{l+1} e^{i[\omega_f t' - m\Phi(t')]} dt', \quad (\text{B9})$$

where the integration is performed on an elliptical orbit with SMA a and eccentricity e . Due to the quick oscillations and the large value of ω_f , numerically evaluating K_f is computationally expensive. [Lai \(1997\)](#) provided an analytical approximation for $l = m = 2$ mode in the parabolic orbit limit where ω_f is much larger than the angular frequency of the orbit at the pericenter. In Appendix C, we generalize their results to elliptical orbits with high eccentricities.

To compute the values of P_k , $K_{f,k}$, $\Delta A_{f,k}$ and complete the iterative map, one must know a_k and e_k , the SMA and the eccentricity between $(k-1)$ -th and k -th pericenter passages. Without oscillation damping, a_k and e_k are

determined by the conservation of the total energy and angular momentum:

$$E_{\text{total}} = E_{\text{orb},k} + E_f = -\frac{GM_b\mu}{2a_k} + |A_{f,k}|^2, \quad (\text{B10})$$

$$L_{\text{total}} = L_{\text{orb},k} + L_f = \mu\sqrt{GM_b a_b(1 - e_k^2)} + \frac{m}{\omega_f} |A_{f,k}|^2, \quad (\text{B11})$$

where $\mu = M_{*,1}M_{*,2}/(M_{*,1} + M_{*,2})$ is the reduced mass of the binary system.

Without pre-existing oscillations, the first inner pericenter passage injects energy $\Delta E_{f,0}$ into f -mode:

$$\Delta E_f = 2\pi^2 \frac{GM_{*,1}^2}{R_{*,1}} \left(\frac{M_{*,2}}{M_{*,1}} \right)^2 \left(\frac{R_{*,1}}{r_p} \right)^{2(l+1)} \bar{Q}_f^2 K_f^2, \quad (\text{B12})$$

which is a very steep function of r_p . The energy injection in the oscillation mode will cause a change in the orbital period:

$$\frac{\Delta P}{P} \approx -\frac{3}{2} \frac{\Delta E_{\text{orb}}}{E_{\text{orb}}} = \frac{3}{2} \frac{\Delta E_{f,0}}{E_{\text{orb}}}. \quad (\text{B13})$$

When the period change is large compared to ω_f ($\Delta\phi = \omega_f \Delta P \gtrsim 1$), the next pericenter passage will introduce a kick in A_f at an effectively random phase. The repeated kicks at random phases over many pericenter passages will result in diffusive and chaotic growth of A_f and E_f . The average energy growth rate is

$$E_f \sim N \Delta E_{f,0}, \quad (\text{B14})$$

where N is the number of inner orbits.

ANALYTIC APPROXIMATION OF THE TEMPORAL OVERLAPPING INTEGRAL FOR ELLIPTICAL ORBITS

Our goal is to analytically compute temporal overlapping integral K (hereafter removing the mode-identity index f) in eq. (B9) at the quadrupolar order $l = 2$ and for the energetically dominating prograde mode with $m = 2$. We consider an elliptical orbit with eccentricity $e < 1$. For a high eccentricity $e \approx 1$, it is convenient to define a small quantity $\epsilon \ll 1$ as follows

$$\epsilon \equiv \frac{1-e}{1+e} \Leftrightarrow e \equiv \frac{1-\epsilon}{1+\epsilon}. \quad (\text{C1})$$

We define a convenient integration variable z based on the true anomaly Φ of the orbit,

$$z \equiv \tan(\Phi/2), \cos \Phi = \frac{1-z^2}{1+z^2}, \sin \Phi = \frac{2z}{1+z^2}, d\Phi = \frac{2dz}{1+z^2}, \quad (\text{C2})$$

and an elliptical orbit with eccentricity e and pericenter radius r_p can be described by

$$\frac{r}{r_p} = \frac{1+e}{1+e \cos \Phi} = \frac{1+z^2}{1+\epsilon z^2}, \quad (\text{C3})$$

and

$$t(z) = \frac{1}{\Omega_p} \int_0^{\Phi} \frac{r^2}{r_p^2} d\Phi = \frac{2}{\Omega_p} \int_0^z \frac{1+z^2}{(1+\epsilon z^2)^2} dz, \quad (\text{C4})$$

where $\Omega_p = L/r_p^2$ is the angular frequency at the pericenter for specific orbital angular momentum L . The key

difficulty in carrying out the time integral in K is the phase factor $\omega t(z)$. Fortunately, one can use the saddle point method to evaluate this integral as long as $\omega \gg \Omega_p$, which is the case in our consideration.

Let us define a dimensionless quantity

$$\lambda \equiv 2\omega/\Omega_p,$$

and the mode oscillation phase factor $i\omega t(z)$ can be described by defining a complex function $h(z)$ as follows

$$i\omega t(z) \equiv \lambda h(z),$$

$$h(z) = \frac{i}{2e^{3/2}} \left[(1+\epsilon) \tan^{-1}(\sqrt{\epsilon}z) - (1-\epsilon) \frac{\sqrt{\epsilon}z}{1+\epsilon z^2} \right]. \quad (\text{C5})$$

For a given mode frequency ω , the temporal overlapping integral K for $l = m = 2$ can be written as

$$\begin{aligned} \frac{\pi}{W_{22}} \frac{\Omega_p}{\Omega_{*,1}} K &= \frac{1}{2} \int_{-\pi}^{\pi} \frac{r_p}{r(\Phi)} e^{i[\omega t(\Phi) + 2\Phi]} d\Phi \\ &= \int_{-\infty}^{+\infty} \frac{1+\epsilon z^2}{1+z^2} \left(\frac{i-z}{i+z} \right)^2 e^{i\omega t(z)} \frac{dz}{1+z^2} \\ &= \int_{-\infty}^{\infty} g(z) e^{\lambda h(z)} dz, \end{aligned} \quad (\text{C6})$$

where we have made use of

$$e^{-2i\Phi} = (\cos \Phi - i \sin \Phi)^2 = [(i+z)/(i-z)]^2, \quad (\text{C7})$$

and defined the complex function $g(z)$,

$$g(z) = \frac{1+\epsilon z^2}{(1+z^2)^2} \left(\frac{i+z}{i-z} \right)^2 = \frac{1+\epsilon z^2}{(z-i)^4}. \quad (\text{C8})$$

Although z is a real physical quantity as it is based on the true anomaly Φ , we consider the final expression in eq. (C6) to be a complex path integral with $z = x + iy$ which is carried out along the real (x) axis of the complex plane — the original path goes from point $A(x = -\infty, y = 0)$ to point $B(x = \infty, y = 0)$. According to Cauchy's residue theorem, we may choose an alternative (arbitrary) path that connects A and B , and the results will be the same as long as the loop formed between the original path (along the real axis) and the alternative path does not enclose any poles of the integrand function $g(z)e^{\lambda h(z)}$.

In the following, we will choose the path where the argument in the exponential term $e^{\lambda h(z)}$ has the steepest descent near a saddle point. When $\lambda \gg 1$ and $h = u(z) + iv(z)$, most of the contribution to the above integral should come from the region where $u(z)$ is maximized while $v(z)$ stays constant (to avoid cancellation due to oscillations). This region must be near where the first derivative $h'(z) = 0$, the solutions to which are the *saddle points* of the function $h(z)$.

Since $h'(z) = (1+z^2)/(1+\epsilon z^2)^2$, we find two saddle points at $z_0 = \pm i$. We will choose $z_0 = i$ as $\text{Re}[h''(z_0)] > 0$ and hence the integral can be converted into the Gaussian form. The 2nd derivative of the function $h(z)$ is given by

$$h''(z) = 2iz \frac{1-2\epsilon-\epsilon z^2}{(1+\epsilon z^2)^3} \quad (\text{C9})$$

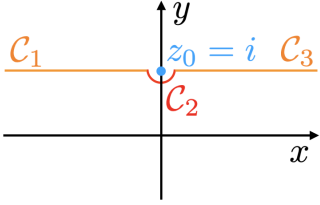


FIG. 15.— The complex integral path $\mathcal{C} = \mathcal{C}_1 + \mathcal{C}_2 + \mathcal{C}_3$ that passes close to the saddle point $z_0 = i$.

and we obtain

$$h''(z_0 = i) = -\frac{2}{(1-\epsilon)^2}, \quad (\text{C10})$$

which is indeed negative. Similarly, we carry out the third derivative and evaluate it at the saddle point $z_0 = i$,

$$h'''(z_0 = i) = 2i \frac{1+7\epsilon}{(1-\epsilon)^3}. \quad (\text{C11})$$

We can also evaluate the original function $h(z)$ at the saddle point in the limit of $\epsilon \ll 1$

$$h(z_0 = i) \approx -\frac{2}{3} \left(1 + \frac{2}{5}\epsilon + \frac{9}{35}\epsilon^2 + \frac{4}{21}\epsilon^3 \right). \quad (\text{C12})$$

The above results allow us to Taylor expand $h(z)$ around $z_0 = i$,

$$\begin{aligned} h(z) &\approx h(z_0) + \frac{h''(z_0)}{2}(z - z_0)^2 + \frac{h'''(z_0)}{6}(z - z_0)^3 \\ &\approx -h_0 - h_2 \tilde{z}^2 + i h_3 \tilde{z}^3, \end{aligned} \quad (\text{C13})$$

where

$$\tilde{z} \equiv z - z_0, \quad (\text{C14})$$

and

$$\begin{aligned} h_0 &\approx \frac{2}{3} \left(1 + \frac{2}{5}\epsilon + \frac{9}{35}\epsilon^2 + \frac{4}{21}\epsilon^3 \right), \\ h_2 &= \frac{1}{(1-\epsilon)^2}, \\ h_3 &= \frac{1}{3} \frac{1+7\epsilon}{(1-\epsilon)^3}. \end{aligned} \quad (\text{C15})$$

Let us also re-write the function $g(z)$ in terms of $\tilde{z} = z - z_0$,

$$g(z) = \tilde{z}^{-4} [1 + \epsilon(\tilde{z} + i)^2] = \sum_{n=0,1,2} g_n i^n \tilde{z}^{n-4}, \quad (\text{C16})$$

where

$$g_0 = 1 - \epsilon, \quad g_1 = 2\epsilon, \quad g_2 = -\epsilon. \quad (\text{C17})$$

Thus, the integral in eq. (C6) can be written as

$$\begin{aligned} I(\lambda, \epsilon) &= \int_{-\infty}^{\infty} g(z) e^{\lambda h(z)} dz \\ &\approx e^{-\lambda h_0} \int_{\mathcal{C}} \left(\sum_{n=0,1,2} g_n i^n \tilde{z}^{n-4} \right) e^{-\lambda h_2 \tilde{z}^2} e^{i \lambda h_3 \tilde{z}^3} dz, \end{aligned} \quad (\text{C18})$$

where the path \mathcal{C} is determined as follows.

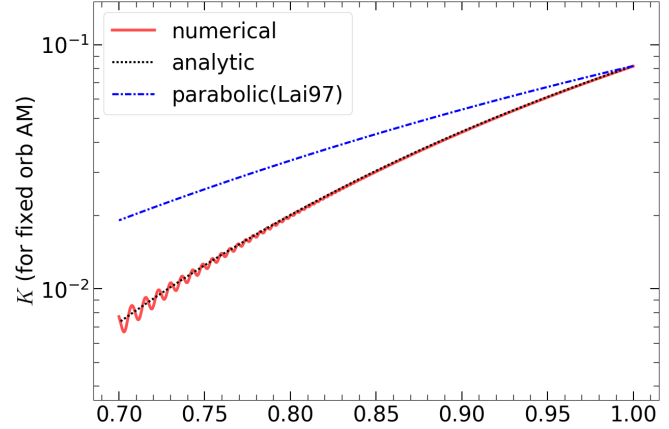


FIG. 16.— Tidal overlap integral K computed using three different methods: direct numerical integration (red solid line), analytic result (eq. C25) from saddle-point method (black dotted line), and the Lai (1997) approximation for parabolic orbit (eq. C26) (blue dash-dotted line). We consider different orbital eccentricities but fix the specific orbital angular momentum such that $r_p(1+e) = 2r_{p,0}$ is conserved. The initial orbit is parabolic with pericenter radius $r_{p,0}$ such that $\lambda_0 = 2\omega/\Omega_{p,0} = 10$, where $\Omega_{p,0} = \sqrt{2GM_{\text{tot}}/r_{p,0}^3}$ is the initial pericenter angular frequency. As the eccentricity evolves, we have $\lambda(e) = 2\omega/\Omega_p = 4(1+e)^2\lambda_0$ for a fixed specific orbital angular momentum.

To avoid rapid oscillations in the Gaussian-like term $e^{-\lambda h_2 \tilde{z}^2}$, we would like to take the path \mathcal{C} to be perpendicular to the imaginary axis. Looking at the polynomial expansion above, we see that the integrand has a pole exactly at the saddle point at $z_0 = i$. For this reason, we slightly change the path into three segments that go around the pole: $\mathcal{C} = \mathcal{C}_1 + \mathcal{C}_2 + \mathcal{C}_3$ as shown in Fig. 15, where \mathcal{C}_1 is a straight line from $-\infty + i$ to $-\rho + i$, \mathcal{C}_2 is a semicircle of infinitesimal radius ρ from $-\rho + i$ to $\rho + i$, and \mathcal{C}_3 is a straight line from $\rho + i$ to $+\infty + i$. The semicircle is taken to be below $z_0 = i$ so the residue at this pole is not involved in the final result. Note that, although the end points of $-\infty + i$ and $+\infty + i$ do not lie on the real axis, this makes little difference as long as most of the contribution to the integral comes from the region near the saddle point $z_0 = i$ — this is the case for highly eccentric orbits.

We further Taylor expand $e^{i \lambda h_3 \tilde{z}^3}$ into polynomials

$$e^{i \lambda h_3 \tilde{z}^3} \approx 1 + i \lambda h_3 \tilde{z}^3, \quad (\text{C19})$$

so the above integral $I(\lambda, \epsilon)$ has six terms (two for each $n = 0, 1, 2$), and we ignore the higher-order ones and retain the following three terms

$$I(\lambda, \epsilon) \approx e^{-\lambda h_0} \int_{\mathcal{C}} \left(\sum_{n=0,1} g_n i^n \tilde{z}^{n-4} + g_0 \tilde{z}^{n-4} i \lambda h_3 \tilde{z}^3 \right) e^{-\lambda h_2 \tilde{z}^2} dz. \quad (\text{C20})$$

We skip the details and write down the results each of the three terms

$$\int_{\mathcal{C}} g_0 \tilde{z}^{n-4} e^{-\lambda h_2 \tilde{z}^2} dz = \frac{4\sqrt{\pi}}{3} g_0 (\lambda h_2)^{3/2}, \quad (\text{C21})$$

$$\int_{\mathcal{C}} i g_1 \tilde{z}^{-2} e^{-\lambda h_2 \tilde{z}^2} dz = \pi g_1 \lambda h_2, \quad (\text{C22})$$

$$\int_C g_0 \tilde{z}^{n-4} i \lambda h_3 \tilde{z}^3 e^{-\lambda h_2 \tilde{z}^2} dz = -\pi g_0 \lambda h_3, \quad (\text{C23})$$

so the integral $I(\lambda, \epsilon)$ is given by

$$I(\lambda, \epsilon) = e^{-\lambda h_0} \left[\frac{4\sqrt{\pi}}{3} g_0 (\lambda h_2)^{3/2} + \pi g_1 \lambda h_2 - \pi g_0 \lambda h_3 \right] \quad (\text{C24})$$

Putting in all the g_n and h_n factors, we obtain the final result for the tidal overlap integral

$$K \approx \frac{4W_{22}}{3\sqrt{\pi}} \frac{\Omega_{*,1}}{\Omega_p} \frac{\lambda^{3/2}}{(1-\epsilon)^2} \left[1 - \frac{\sqrt{\pi}}{4} (1+\epsilon) \lambda^{-1/2} \right] \times \exp \left[-\frac{2}{3} \left(1 + \frac{2}{5}\epsilon + \frac{9}{35}\epsilon^2 + \frac{4}{21}\epsilon^3 \right) \lambda \right], \quad (\text{C25})$$

where we find that $9\epsilon^2/35 + 4\epsilon^3/21$ are important as they are in the exponential argument but that the higher-order terms⁶ $\mathcal{O}(\lambda^{-1})$ are negligible for sufficiently large $\lambda \gtrsim 10$. Our result (eq. C25) is also in agreement with that of Lai (1997) in the limit $\epsilon = 0$,

$$K(\epsilon = 0) \approx \frac{4W_{22}}{3\sqrt{\pi}} \frac{\Omega_{*,1}}{\Omega_{p,\text{PT}}} \lambda_{\text{PT}}^{3/2} \left(1 - \frac{\sqrt{\pi}}{4} \lambda_{\text{PT}}^{-1/2} \right) e^{-2\lambda_{\text{PT}}/3}, \quad (\text{C26})$$

where the angular frequency at the pericenter $\Omega_{p,\text{PT}}$ is for a parabolic orbit as considered by Press and Teukolsky (1977)

$$\Omega_{p,\text{PT}} = \sqrt{\frac{2G(M_{*,1} + M_{*,2})}{r_p^3}}, \quad \lambda_{\text{PT}} \equiv \frac{2\omega}{\Omega_{p,\text{PT}}}. \quad (\text{C27})$$

For an elliptical orbit with the same pericenter radius r_p , the physical pericenter frequency is

$$\Omega_p = \sqrt{\frac{(1+e)G(M_{*,1} + M_{*,2})}{r_p^3}} = \sqrt{\frac{1+e}{2}} \Omega_{p,\text{PT}}, \quad (\text{C28})$$

and the mode frequency ratio is $\lambda = 2\omega/\Omega_p = \sqrt{2/(1+e)}\lambda_{\text{PT}}$.

SECOND-ORDER PERTURBATION OF THE BINARY SYSTEM

We provide below the expression of the second-order eccentricity perturbation of a binary system by the MBH using secular approximation in the parabolic orbit limit. Readers are referred to Hammers and Samsing (2019) for the derivation and more details. Here we only state the result for parabolic orbits in high perturber mass limit.

The inner eccentricity vector of the binary system prior to the perturbation is

$$\mathbf{e}_b = e_x \hat{\mathbf{x}} + e_y \hat{\mathbf{y}} + e_z \hat{\mathbf{z}} \quad (\text{D1})$$

$$= \frac{1}{GM_b} \dot{\mathbf{r}}_b \times (\mathbf{r}_b \times \dot{\mathbf{r}}_b) - \hat{\mathbf{r}}_b, \quad (\text{D2})$$

where \mathbf{r}_b is the separation between the binary. The normalized angular momentum vector $\mathbf{j}_b = j_x \hat{\mathbf{x}} + j_y \hat{\mathbf{y}} + j_z \hat{\mathbf{z}}$

⁶ Getting the next order $\mathcal{O}(\lambda^{-1})$ is quite involved, as one must include 4th order derivative in $h(z)$, the $n = 2$ term in $g(z)$, and the 2nd order expansion of $e^{i\lambda h_3 \tilde{z}^3}$ above.

is in the direction $\mathbf{r}_b \times \dot{\mathbf{r}}_b$ and has magnitude $\sqrt{1 - e_b^2}$. The scale of eccentricity perturbation is controlled by the parameter ϵ_{SA} :

$$\epsilon_{\text{SA}} = \left[\frac{1}{8} \frac{M_{\text{BH}}}{M_b} \left(\frac{a_b}{r_p} \right)^3 \right]^{1/2} = \frac{1}{2\sqrt{2}} \left(\frac{r_t}{r_p} \right)^{3/2}. \quad (\text{D3})$$

For the outer orbit in xy plane and outer pericenter in -x direction, the total perturbation to $\mathbf{e}_b, \mathbf{j}_b$ are

$$\Delta \mathbf{e}_b = \epsilon_{\text{SA}} \mathbf{f}_e + \epsilon_{\text{SA}}^2 \mathbf{g}_e, \quad (\text{D4})$$

$$\Delta \mathbf{j}_b = \epsilon_{\text{SA}} \mathbf{f}_j + \epsilon_{\text{SA}}^2 \mathbf{g}_j, \quad (\text{D5})$$

where

$$\mathbf{f}_e = -\frac{3\pi}{2} (3e_z j_y + e_y j_z) \hat{\mathbf{x}} + \frac{3\pi}{2} (3e_z j_x + e_x j_z) \hat{\mathbf{y}} + 3\pi (e_y j_x - e_x j_y) \hat{\mathbf{z}}, \quad (\text{D6})$$

$$\mathbf{f}_j = -\frac{3\pi}{2} (5e_y e_z - j_y j_z) \hat{\mathbf{x}} + \frac{3\pi}{2} (5e_x e_z - j_x j_z) \hat{\mathbf{y}}, \quad (\text{D7})$$

$$\begin{aligned} \mathbf{g}_e = & \frac{3}{16} \pi \left[75e_x^2 e_y - 6\pi (e_x (15e_z^2 - 6j_y^2 + j_z^2) + 6e_y j_x j_y) \right. \\ & + 50e_y^3 + 5e_y (10e_z^2 + j_x^2 - 10(j_y^2 + 2j_z^2)) + 50e_z j_y j_z \left. \hat{\mathbf{x}} \right] \\ & - \frac{3}{16} \pi \left[75e_x^3 + e_x (50e_y^2 + 5j_x^2 + 36\pi j_x j_y - 150j_z^2) \right. \\ & + 6\pi e_y (15e_z^2 - 6j_x^2 + j_z^2) - 10j_x (5e_y j_y + e_z j_z) \left. \hat{\mathbf{y}} \right] \\ & + \frac{3}{8} \pi \left[-6\pi e_z (5e_x^2 + 5e_y^2 - 3(j_x^2 + j_y^2)) \right. \\ & - 5(5e_x e_y e_z + 15e_x j_y j_z - 9e_y j_x j_z + 5e_z j_x j_y) \\ & \left. + 12\pi j_z (e_x j_x + e_y j_y) \right] \hat{\mathbf{z}}, \end{aligned} \quad (\text{D8})$$

$$\begin{aligned} \mathbf{g}_j = & \frac{3}{16} \pi \left[75e_x^2 j_y + 60\pi e_x e_y j_y - 6\pi j_x (10e_y^2 + 15e_z^2 + j_z^2) \right. \\ & - 50e_y e_z j_z + 50e_z^2 j_y + 5j_x^2 j_y \left. \hat{\mathbf{x}} \right] \\ & - \frac{3}{16} \pi \left[15e_x^2 (5j_x + 4\pi j_y) \right. \\ & - 10e_x (6\pi e_y j_x + 5e_y j_y + 15e_z j_z) \\ & \left. + 5j_x (10e_y^2 + j_x^2 - 2j_z^2) + 6\pi j_y (15e_z^2 + j_z^2) \right] \hat{\mathbf{y}} \\ & - \frac{15}{8} \pi [5e_x e_y j_z + 5e_x e_z j_y + 5e_y e_z j_x + j_x j_y j_z] \hat{\mathbf{z}}. \end{aligned} \quad (\text{D9})$$

Note that in our models, the outer orbits do not necessarily lie on the xy plane. In those cases, proper coordinate rotations are first performed before applying the above perturbation results.

ORBITAL CIRCULARIZATION DUE TO DAMPING OF DYNAMICAL TIDES

In the following we modify the results in Barker (2020) based on physical arguments to roughly estimate the dynamical tides timescale of binaries $t_{a,\text{dyn}}$ after the chaotic tides.

Consider the tidal dissipation in only one star of the binary of equal mass. The circularization timescale in a

low-eccentricity limit is estimated to be (Barker 2020)

$$t_{e,\text{Barker}} = \frac{2^{8/3}}{63\pi} Q' \frac{P_b^{13/3}}{P_{\text{dyn}}^{10/3}}, \quad (\text{E1})$$

where $P_{\text{dyn}} = 2\pi\sqrt{a_b^3/(GM_b)}$ is the period associated with the dynamical time of the star, and Q' is the modified tidal quality factor. Here we consider the tidal damping from inertial waves, with the corresponding Q' (Barker 2020):

$$Q' = Q'_{\text{IW}} \approx 10^7 \left(\frac{P_{\text{rot}}}{10 \text{ d}} \right)^2, \quad (\text{E2})$$

where P_{rot} is the rotation period of the star. For our binaries after the chaotic tides, there are two main differences. First, the high eccentricities of the binaries will limit the tidal interactions to close to the pericenter and reduce the overall efficiency of the circularization. We account for this effect by scaling $t_{e,\text{Barker}}$ with the ratio of the orbital period to the time near the pericenter:

$$t_{a,\text{dyn}} = t_{e,\text{Barker}} \left(\frac{a_b}{r_{p,b}} \right)^{3/2}. \quad (\text{E3})$$

Second, while stars in a small-eccentricity binary tend to reach the synchronous rotation with the orbit, the high residual eccentricity in binaries after the chaotic tides will cause the star to spin near the orbital angular frequency at the pericenter. We therefore set P_{rot} to be

$$P_{\text{rot}} = 2\pi \sqrt{\frac{r_{p,b}^3}{GM_b(1+e_b)}}. \quad (\text{E4})$$

Using binary conditions after chaotic tides (Figure 14), we find that the dynamical tides timescale is less than one outer orbital period. We emphasize that this extrapolation of $t_{a,\text{dyn}}$ to highly eccentricities has huge uncertainties and is only meant to demonstrate the power of dynamical tides.

This paper was built using the Open Journal of Astrophysics L^AT_EX template. The OJA is a journal which provides fast and easy peer review for new papers in the **astro-ph** section of the arXiv, making the reviewing process simpler for authors and referees alike. Learn more at <http://astro.theoj.org>.